# Modulated ringdown comb interferometry for sensing of highly complex gases

https://doi.org/10.1038/s41586-024-08534-2

Received: 4 June 2024

Accepted: 17 December 2024

Qizhong Liang[1]✉, Apoorva Bisht[1], Andrew Scheck[1], Peter G. Schunemann[2,3] & Jun Ye[1]✉

Gas samples relevant to health[1–3] and the environment[4–6] typically contain many molecular species that span a huge concentration dynamic range. Mid-infrared frequency comb spectroscopy with high-finesse cavity enhancement has allowed the most sensitive multispecies trace-gas detections so far[2,7–13]. However, the robust performance of this technique depends critically on ensuring absorption-path-length enhancement over a broad spectral coverage, which is severely limited by comb–cavity frequency mismatch if strongly absorbing compounds are present. Here we introduce modulated ringdown comb interferometry, a technique that resolves the vulnerability of comb–cavity enhancement to strong intracavity absorption or dispersion. This technique works by measuring ringdown dynamics carried by massively parallel comb lines transmitted through a length-modulated cavity, making use of both the periodicity of the field dynamics and the Doppler frequency shifts introduced from a Michelson interferometer. As a demonstration, we measure highly dispersive exhaled human breath samples and ambient air in the mid-infrared with finesse improved to 23,000 and coverage to 1,010 cm$^{-1}$. Such a product of finesse and spectral coverage is orders of magnitude better than all previous demonstrations[2,7–20], enabling us to simultaneously quantify 20 distinct molecular species at above 1-part-per-trillion sensitivity varying in concentrations by seven orders of magnitude. This technique unlocks next-generation sensing performance for complex and dynamic molecular compositions, with scalable improvement to both finesse and spectral coverage.

Achieving the most sensitive multispecies trace-gas sensing is critical for many frontier applications, including precise determination of complex molecular structures[9,11], real-time reaction kinetics[12,13], atmospheric sensing[4–6] and breath-based medical diagnostics[1–3]. An enhancement cavity[21] formed by a pair of high-reflectivity optical mirrors is a powerful tool for this goal, as it enables light to circulate through the same sample to substantially enhance the absorption path length for sensing the weakest absorption signals. However, laser light cannot be coupled through a cavity unless the laser frequency is precisely matched to a cavity resonance, that is, the optical frequency corresponding to accumulating a cavity round-trip phase delay equal to integer multiples of 2π (Fig. 1a). A large set of cavity resonances are established with varying spectral gaps between each other caused by intracavity dispersion arising from the refractive index of loaded gas samples and mirror reflection.

Enabling cavity enhancement with broadband spectral coverage for multispecies detection requires the use of optical frequency combs, a type of broadband laser that consists of many narrow-linewidth optical lines (that is, comb lines) emitted at strictly evenly spaced frequencies. All comb lines can sequentially and deterministically couple through the cavity if each of them is swept across a cavity resonance at sufficient modulation depth (Fig. 1b). Normally measured with a grating monochromator for experiments conducted in the near-infrared[22], the ringdown time $\tau_{\mathrm{RD}}$ characterizing the temporal width of the cavity transmitted burst reflects the number of round trips laser light can circulate within the cavity. This forms the basics of cavity ringdown spectroscopy[23] for ultra-sensitive detection of intracavity absorption from the loaded samples. Yet, such a normal scheme is challenging to extend to the mid-infrared owing to the present mid-infrared photodetection technologies lacking detectivity and speed[12–14].

Here we introduce modulated ringdown comb interferometry (MRCI), a variant of ringdown interferometry methods[24,25], to realize unrestricted comb–cavity enhancement across an unprecedented spectral range in the mid-infrared. We present the simple use of a standard Michelson interferometer, commonly believed to be restricted to measuring laser fields with static intensity in time, as a superior spectrometer for measuring comb's intensity dynamics generated from the transient comb–cavity coupling scheme. The critical concept is to measure temporal dynamics in the Fourier frequency domain, in which reflection from a moving mirror in a Michelson interferometer is used to offset the Fourier harmonics frequencies decomposing the periodically generated intensity dynamics. As a result, each comb line is engineered to be measured at isolated radio frequencies of $n\omega_m + \omega_i$, with $n$ a list of integers representing Fourier harmonics orders, $\omega_m$ the cavity length modulation rate and $\omega_i$ the Doppler frequency shift. Because the same $\omega_m$ but different $\omega_i$ are engineered for different comb lines, intensity dynamics can be parallelly observed for different comb

---

[1]JILA, National Institute of Standards and Technology and University of Colorado, Boulder, CO, USA. [2]BAE Systems, Nashua, NH, USA. [3]Present address: Onsemi, Hudson, NH, USA. ✉e-mail: Qizhong.Liang@colorado.edu; Ye@jila.colorado.edu

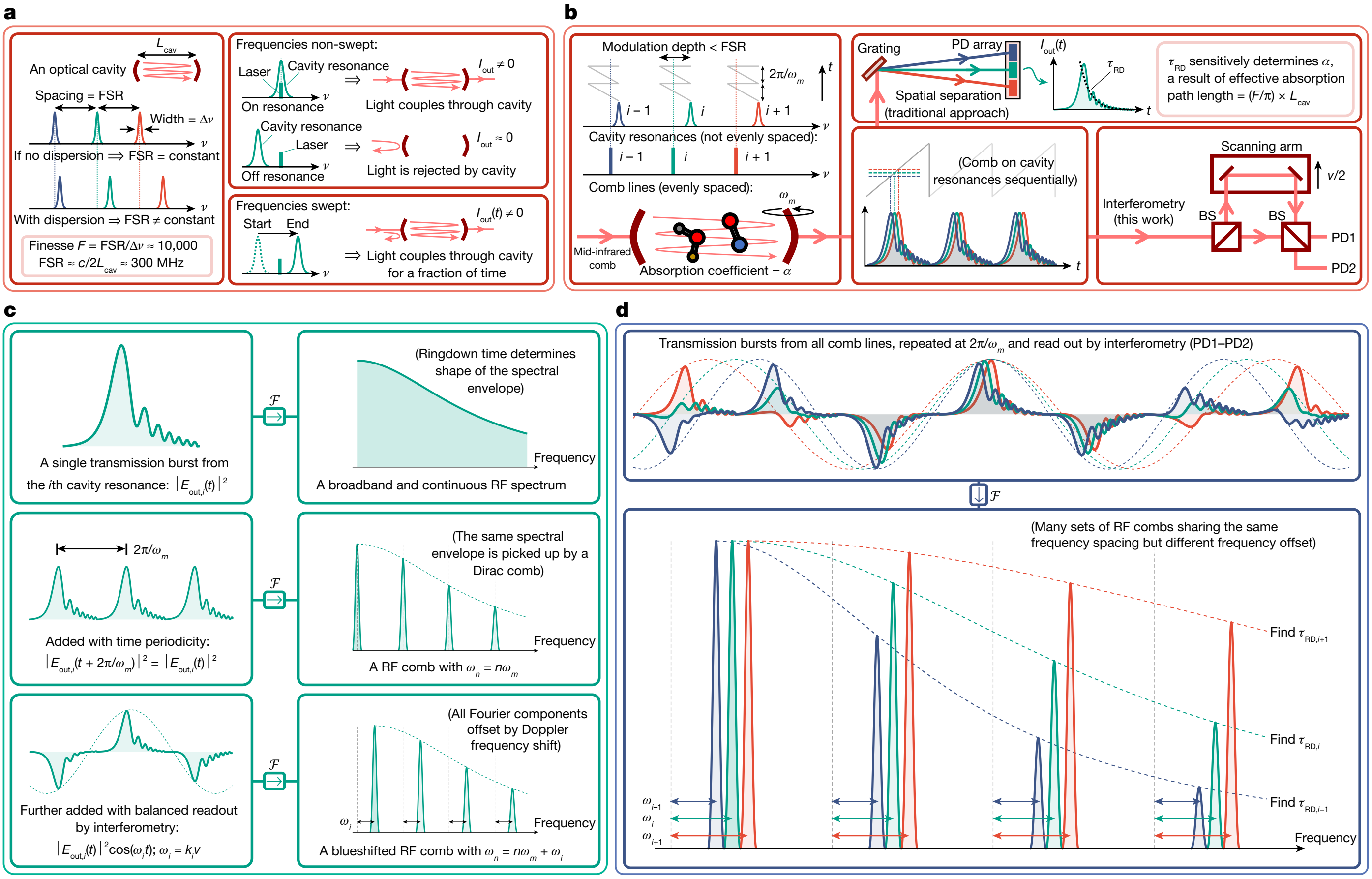

**Fig. 1 | MRCI. a**, An optical cavity formed by a pair of high-reflectivity mirrors enables marked enhancement in light-molecule absorption path length. Finesse and free spectral range (FSR) are two quantities respectively characterizing the frequency width and spacing of the cavity resonances formed from the field boundary conditions. Their typical values are given. A larger cavity finesse leads to narrower cavity resonances but provides stronger enhancement to the absorption path length. A continuous-wave laser must be precisely matched to a cavity resonance in optical frequency to be coupled through the cavity. Dispersion originated from the loaded gas molecules and mirror spectral response can displace the frequency of the cavity resonances (Methods). **b**, A high-finesse cavity periodically modulated in cavity length permits an incident mid-infrared comb to transmit through the cavity once per cavity length sweep. Within a single sweep, laser fields from different cavity resonances are transmitted sequentially. Traditionally, the periodic cavity transmission bursts are read out by a photodetector (PD) array following grating separation. Fitting to the temporal envelope yields ringdown time that ultra-sensitively probes the intracavity absorption. In this work, instead, we use a passively scanning Michelson interferometer for spectroscopy readout. **c**, Physical interpretations of the recorded interferogram. Shown are the intensity subcomponents versus time generated from a particular cavity resonance. Through the addition of time periodicity and readout by interferometry, the spectral information generated by the same cavity resonance is engineered into an ‘RF spectral comb’ with frequency spacing given by cavity length modulation frequency, frequency offset given by the Doppler frequency shift and a spectral envelope determined by the ringdown time. **d**, Fourier transform of the recorded interferogram thus encompasses a series of RF spectral combs spectrally isolated from each other for simultaneous broadband high-resolution ringdown measurements. For simplicity in the discussion, the emission rate of cavity transmission bursts and Doppler frequency shift are assumed here to be constants. This is not a mandatory requirement in experimental realizations: their lack of mutual coherence can be robustly tackled with data-reconstruction methods. See Methods for details. BS, beam splitter.

lines free from spectral overlap. Broadband ringdown spectroscopy down to comb-mode resolution can thus be realized.

Practical utility for real-world sensing tasks[26–30] requires the sensing tool to be robust over long-term operations and, at the same time, exhibit extreme performance to thoroughly quantify different species present in a gas sample. In MRCI, the transient comb–cavity coupling scheme brings general applicability to sensing real-world samples containing previously unknown, highly complex and dynamic molecular contents. With dispersion immunity, scalable enhancement for both cavity finesse and spectral coverage can be achieved. Our new apparatus realized with much improved finesse–spectral coverage product (Fig. 2) showcases a new capability to navigate through intense absorption features from molecules including $H_2O$, HDO, $CH_4$, $CO_2$ and $N_2O$ to detect the lowest-concentration species (hydrocarbons, alcohols, nitric oxide, aldehyde, ketone and others) at sensitivity down to a few parts per trillion (100 times improvement[2]). Simple operations using free-running frequency combs without any high-bandwidth feedback loops make possible highly automated and efficient data collection to bring practicality for large-scale measurements. In the following, we detail the working principle of MRCI and demonstrate its performance over exhaled breath and ambient air.

## MRCI

MRCI encompasses two essential ingredients: (1) a high-finesse cavity swept-locked to the incident mid-infrared comb to permit its periodic transmission through the cavity once per cavity length sweep and (2) an asynchronous, passively scanning Michelson interferometer to read out the periodic cavity transmission bursts through balanced detection.

Divided into steps (Fig. 1c), we present how the recorded interferogram as a function of time allows high-spectral-resolution

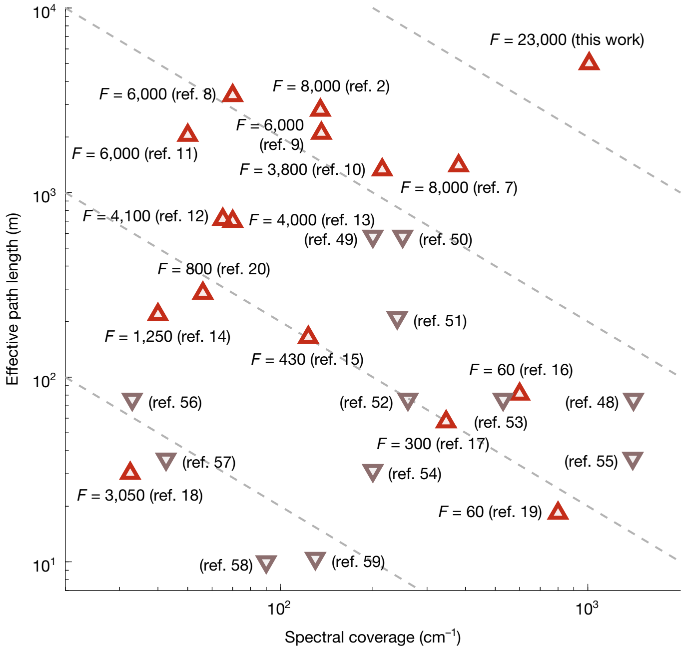

**Fig. 2 | Extreme-performance multispecies trace-gas sensing.** A larger spectral coverage in the mid-infrared region (2–20 μm) enables more molecular species to be identified, whereas a larger effective absorption path length enables molecules of lower concentrations to be detected. Summarized[2,7–20,48–59] are apparatus demonstrated with spectroscopy results performed over 10 cm$^{-1}$ coverage and over 10 m effective path length. Only tabletop mid-infrared frequency comb spectroscopy experiments are considered. For all plotted data points, experiments performed with enhancement cavities (or multipass cells) are labelled with up-pointing (or down-pointing) triangles in red (or grey) colour. Maximum cavity finesse is indicated for experiments using enhancement cavities. The dashed lines indicate trends at constant product between effective path length and spectral coverage.

determination of the ringdown time spectrum. Step 1: consider a single transmission intensity burst generated from the *i*th cavity resonance. Related by a Fourier transformation, the shape of the spectral envelope uniquely determines the ringdown time. A shorter ringdown time corresponds to a flatter spectral envelope. Step 2: record the same transmission bursts repeatedly at a periodicity $2\pi/\omega_m$: the original spectral information is now transformed into a set of Fourier components spaced by $\omega_m$. Step 3: record the same periodic transmission bursts through balanced detection from a Michelson interferometer. All Fourier components are frequency-displaced with a corresponding Doppler frequency shift that is proportional to the *i*th cavity resonance wavenumber and velocity of the delay stage. The spectral information for this cavity resonance is thus engineered into an 'RF spectral comb', with a spacing of $\omega_m$ and spectral intensity distribution determined by the cavity ringdown time. RF spectral combs generated from optical comb components transmitted through different cavity resonances share the same spacing $\omega_m$ but with discrete frequency offsets (Fig. 1d). Determination of the spectral intensity distributions for different sets of RF spectral combs thus realizes broadband simultaneous ringdown measurements. For a complete discussion of MRCI, see Methods and Extended Data Figs. 1–4.

The dispersion immunity brought by MRCI allows scalable expansion of spectral coverage up to the full mirror coating range of high-finesse cavities. In our newly constructed apparatus, we used two high-finesse cavities with axes intersected to probe the same gas sample (Fig. 3a). One cavity permits spectroscopic data collection over the 1,850–2,230-cm$^{-1}$ wavenumber range (near 5 μm in wavelength; finesse peaks at 23,000; ringdown time peaks at 17 μs), the other at the 2,700–3,330-cm$^{-1}$ range (near 3 μm in wavelength; finesse peaks at 14,000; ringdown time peaks at 8 μs). Data collection for either cavity is highly automated (Methods). The comb source used for the 5-μm cavity is a newly constructed, synchronously pumped, singly resonant optical parametric oscillator (OPO) using a type I phase-matched zinc germanium phosphide crystal (Methods and Extended Data Fig. 5). The 3-μm cavity is probed with a previously reported OPO comb[31].

## Demonstration in spectroscopic sensing

We demonstrate MRCI with measurements of exhaled breath collected from nasal and oral respiratory airways and ambient air (see Methods for sampling protocols). The new record-level finesse and broadband coverage allow us to accurately quantify subtle differences in these complex gas samples for a comprehensive list of trace molecular species. Notably, nitric oxide, the species with administrative approval for asthma monitoring, can now be robustly measured on top of the strongly saturated water absorption background and down to its extremely low concentration of about 20 ppb (ref. 32).

Sample data collected with 2 s of acquisition time with the cavity filled with an exhaled breath sample using MRCI are presented in Fig. 3b. Trend lines in red highlight the two sets of Fourier components generated at two different optical frequencies. Insets show the fitted ringdown values. A faster decrease in spectral intensities with the increase of Fourier harmonics order corresponds to a longer cavity ringdown time. Measured for the same breath sample, the full-coverage ringdown spectrum determined from the 5-μm cavity is presented in Fig. 3c and that from the 3-μm cavity is presented in Fig. 3d. Comparing the ringdown data measured with cavity loaded with breath against that measured with empty cavity (held at base pressure below 3 mTorr), the reduction in the ringdown time as a function of optical frequency yields many molecular absorption features generated uniquely from the loaded breath molecules inside the cavity. Ringdown data measured for the empty 5-μm cavity correspond to water absorption signals at below 2,000 cm$^{-1}$, arising from residual water molecules present inside the cavity. The ringdown spectrum measured for the empty 3-μm cavity was found to exhibit large but slowly varying reflectivity oscillating at a period of about 300 cm$^{-1}$ wavenumbers, a feature that is likely a result of the mirror coating design. For both cavities, neither the intracavity dispersion from the non-flat mirror spectral response nor the strong molecular absorptions prevent us from using the entire range of high-reflectivity coating for ultra-sensitive absorption spectroscopy.

Ringdown data collected for various gas samples are referenced against the empty cavity data for the determination of the molecular absorption spectra. Data collected from the 5-μm and 3-μm cavities are presented in Figs. 4a and 5a, respectively. Global molecular fitting results to the HITRAN database are plotted as inverted features. Zoom-ins to discrete spectral regions, in which individual molecular fit results are plotted with colour to highlight absorption features from nitric oxide (NO), carbon monoxide isotopologue ($^{13}$CO), formaldehyde ($H_2CO$) and methanol ($CH_3OH$), as shown in Figs. 4b,c and 5b,c, respectively. For nitric oxide and formaldehyde, their absorption features are much stronger in nasal breath samples but weaker and similar in both oral breath and ambient air. The absorption features of $^{13}$CO and methanol are visually less contrasting between nasal and oral breaths but considerably more intense than that from the air sample. For these extremely low-concentration molecular species, it can be clearly seen that their weak absorption features are highly overlapped with absorption features from other strongly absorbing species, yet they are robustly measured by MRCI with immunity to cavity dispersion issues.

Molecular cross-section data totalling 20 species are fitted to the experimental data. Summarized in Fig. 6, we identified greatly increased concentrations for several species in nasal breath compared with oral breath. We attribute the results for nitric oxide[32,33] and carbon monoxide isotopologues (CO, $^{13}$CO) (ref. 34) to the production in the

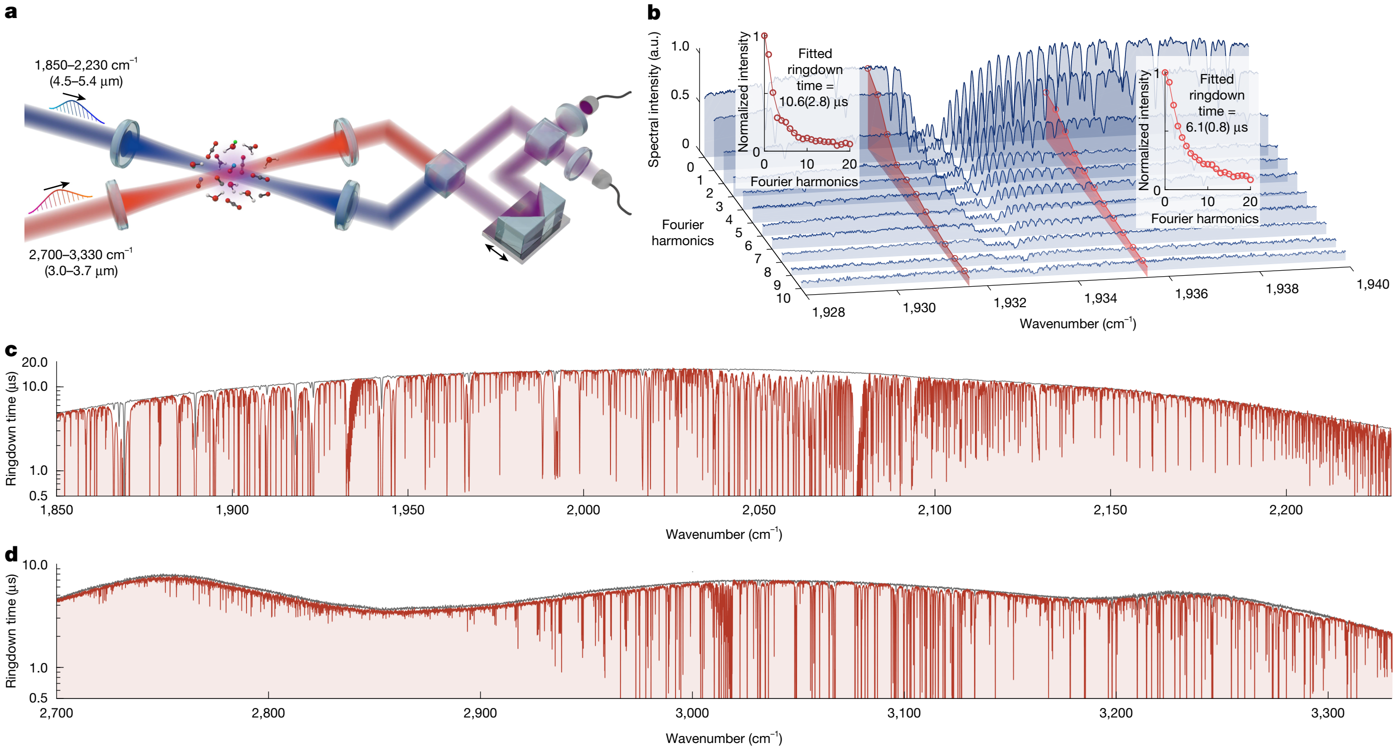

**Fig. 3 | Apparatus and survey ringdown spectra collected with MRCI.** **a**, Apparatus: two sets of high-finesse cavities are used for probing the same gas sample. One at 5-μm wavelength range (finesse peaks at 23,000) permits spectral output between 1,850 cm$^{-1}$ and 2,230 cm$^{-1}$, the other at 3-μm wavelength range (finesse peaks at 14,000) permits spectral output between 2,700 cm$^{-1}$ and 3,330 cm$^{-1}$. **b**, Sample spectral data processed from the recorded interferogram data collected at 2 s acquisition time, 800 MHz instrument resolution, with the cavities loaded with a breath sample. Trend lines in red highlight Fourier components from different cavity resonances. The trend of decay in spectral intensities with the increase of Fourier harmonics order is fitted to an analytically derived formula (Methods) to determine the ringdown time. Insets show the fitted ringdown times, in which circles are experimental data and solid lines are the fitted curves. **c**,**d**, Survey ringdown spectra measured for the same breath samples (red) using the two sets of cavities. Data in black show the ringdown data measured for cavity held at base pressure (below 3 mTorr). The decrease in ringdown times in data measured for breath from that measured for cavity at base pressure determine the molecular absorption signals generated from the loaded breath sample. a.u., arbitrary units.

paranasal sinuses, water isotopologue to the supply from the mucous membrane and acetone plausibly owing to their high water-solubility and thus carried out more by the increased water contents in the nasal airway. On the other hand, the increase in nitrous oxide ($N_2O$) in the oral breath might arise from production by denitrifying bacteria present in the oral cavity[35]. We note that molecular profiles measured from nasal and oral breaths probably vary from one participant to the next and may change depending on the sampling methods and their actual execution. This study focuses primarily on reporting the new capabilities for characterizing highly dispersive gas samples. Nevertheless,

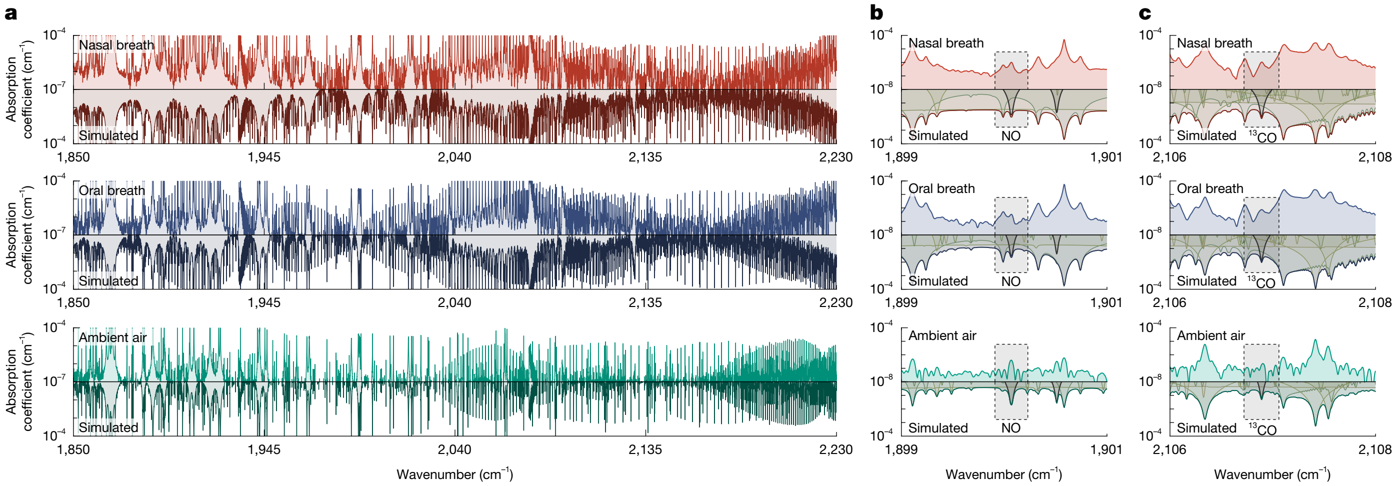

**Fig. 4 | Molecular spectroscopy from the 5-μm cavity.** Shown are nasal breath (red; first row), oral breath (blue; second row) and ambient air (green; third row). **a**, Spectroscopy data from 1,850 cm$^{-1}$ to 2,230 cm$^{-1}$. Experimental data are compared with the global fit results plotted inverted in sign by darkened colours. **b**,**c**, Zoom-ins to individual spectral ranges. Fit results from individual molecules are plotted along with global fit results. Absorption features from nitric oxide (NO) in **b** and carbon monoxide isotopologue ($^{13}$CO) in **c** are highlighted in black.

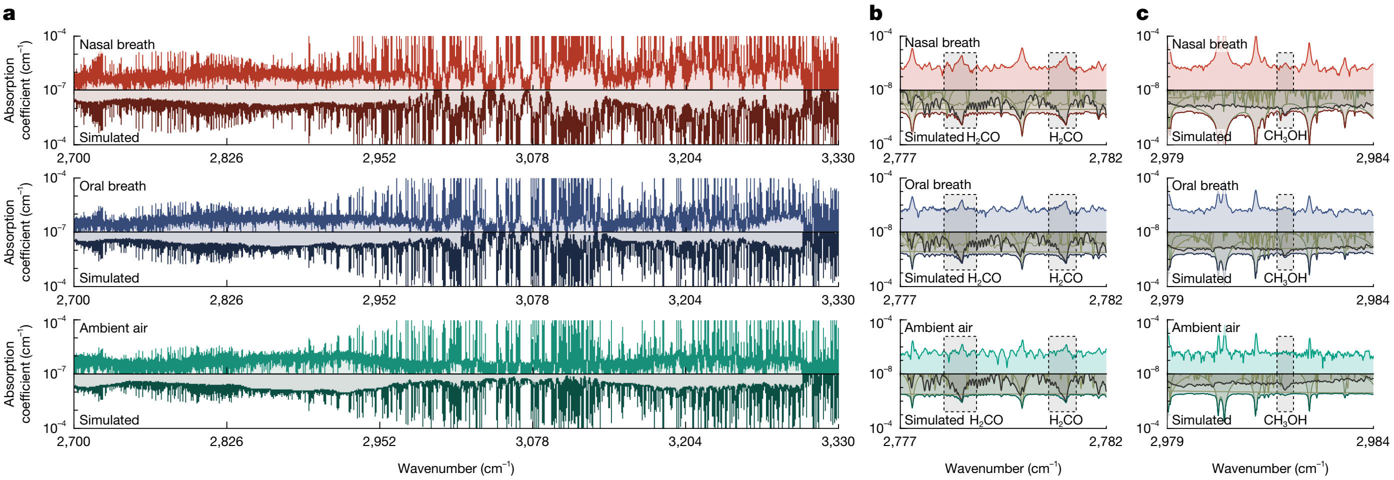

**Fig. 5 | Molecular spectroscopy from the 3-µm cavity.** Shown are nasal breath (red; first row), oral breath (blue; second row) and ambient air (green; third row). **a**, Spectroscopy data from 2,700 cm$^{-1}$ to 3,330 cm$^{-1}$. Experimental data are compared with the global fit results plotted inverted in sign by darkened colours. **b**,**c**, Zoom-ins to individual spectral ranges. Fit results from individual molecules are plotted along with global fit results. Absorption features from formaldehyde ($H_2CO$) in **b** and methanol ($CH_3OH$) in **c** are highlighted in black.

this powerful capability has allowed us to establish a broader utility to simultaneously observe a rich variety of biological conditions through non-invasive measurements of breath.

Comparing our breath measurement results with that of air, carbon dioxide isotopologues ($CO_2$, $^{13}CO_2$, $OC^{18}O$, $OC^{17}O$), water isotopologues ($H_2O$, $H_2{}^{18}O$, $H_2{}^{17}O$ and HDO), methane isotopologues ($CH_4$, $^{13}CH_4$) and carbon monoxide isotopologues (CO, $^{13}CO$) measured from the breath samples are strongly increased. The increase in methane confirms the participant as a methane producer, a result of excess archaea microbiome present in the small intestine[36]. The typical concentrations of the fitted molecular species measured for healthy controls reported by the literature are listed by circles on the stem lines in Fig. 6. They generally agree well with our measurement results. Yet, the formaldehyde concentrations measured at >100 ppb are considerably larger than that normally expected at below 10 ppb in the present literature[37,38]. Formaldehyde is a common air pollutant[39] and known to outgas from chamber surfaces[40]. Further investigation will be needed to interpret the high concentrations measured in this study. Normalized to the acquisition time of 100 s, molecular concentration sensitivities into the parts-per-trillion levels (below 1 ppb) are found for 15 out of the 20 molecules and are summarized by the open squares on the stem lines in Fig. 6. The best sensitivity at 8 ppt is obtained for $N^{15}NO$ and $^{15}NNO$. The minimum detectable absorption (MDA) at 1 s per spectral element is $3 \times 10^{-10}$ cm$^{-1}$ Hz$^{-1/2}$ for the 5-µm cavity and $6 \times 10^{-10}$ cm$^{-1}$ Hz$^{-1/2}$ for the 3-µm cavity. More details on evaluating detection sensitivity and on molecular line fitting can be found in Methods.

## Discussion

When in the absence of intracavity dispersion, traditional methods of interferometry readout of static laser fields generated from tight comb–cavity coupling (that is, concurrent matching frequencies of different comb lines to different cavity resonances) can be used[2,41,42]. Detection sensitivity down to the quantum shot noise limit can be achieved in the near-infrared benefiting from the availability of ultralow-noise photodetectors[42]. MRCI is a new spectroscopy technique invented for the necessity to enable practical measurement of gas samples of arbitrary dispersion profile. For measurements of exhaled breath and ambient air in the mid-infrared molecular fingerprint region, displacement of cavity resonance frequencies occurs in a range amounting to more than 100 times the cavity resonance width even for modest cavity finesse at 1,000 (Extended Data Fig. 2 and Methods). Tight comb–cavity coupling must be replaced with transient coupling schemes and ringdown detection is used as a sensitive method for probing intracavity absorption.

The traditional ringdown detection scheme based on grating monochromators[22] is not practical in the mid-infrared primarily because of the slow integration time (≥10 µs) of detector arrays to resolve ringdown dynamics[12–14]. Sensing intracavity absorption is instead based on measuring the cavity-transmitted power rather than ringdown. Highly dispersive, virtually imaged phase array etalons are required to achieve sufficient spectral resolution (<1 GHz) and the instantaneous spectral coverage is compromised to well below 100 cm$^{-1}$, limited by the size of the detector arrays. High optical power loss and strong detection noise floor impose further technological restrictions to achieving the highest possible detection sensitivity. Recent reports[24,25] on using interferometry for implementing ringdown detection in the near-infrared commonly necessitate the use of tight comb–cavity coupling: high coherence control must be achieved either for ringdown events generation[25] or for the interferometry scan[24]. Although spectral resolution below 1 GHz can be achieved, spectral coverages are compromised to <50 cm$^{-1}$ and finesse-coverage products are more than 60 times below that available with standard grating monochromators[22]. The trade-off in spectral coverage, cavity finesse and spectral resolution of previous techniques[22,24,25] prevent the development of more extreme sensing capability. This long-standing bottleneck is resolved by MRCI, which makes it possible for extensive compound determination for real-world gas samples, which are often highly dispersive and contain unknown chemical compounds.

Yet, for the technique to be practically usable in real-world, large-scale settings, equal emphasis must be placed on robustness and simplicity. In MRCI, the occurrence frequency of cavity transmission bursts $\omega_m$ and the Doppler frequency shift $\omega_i$ must have their frequency mixed signals ($n\omega_m + \omega_i$, $n$ is an integer; Fig. 1d) accurately determined free from spectral overlap for broadband ringdown detection. The $\omega_m$ is real-time-perturbed by comb–cavity frequency detuning, cavity length piezo hysteresis and intracavity dispersion (Extended Data Figs. 1 and 2), whereas $\omega_i$ is real-time-perturbed by mechanical stage moving jitter. We show that accurate detection of frequency mixed signals can directly be achieved through data analysis of the collected interferogram. Two pivotal data-reconstruction methods, pulse pairing and demodulation, are introduced and detailed in Methods and Extended Data Fig. 3. Spectroscopy data collection can thus be executed despite the lack of mutual coherence between ringdown generation and interferometry scan. MRCI thus does not require comb frequencies to be

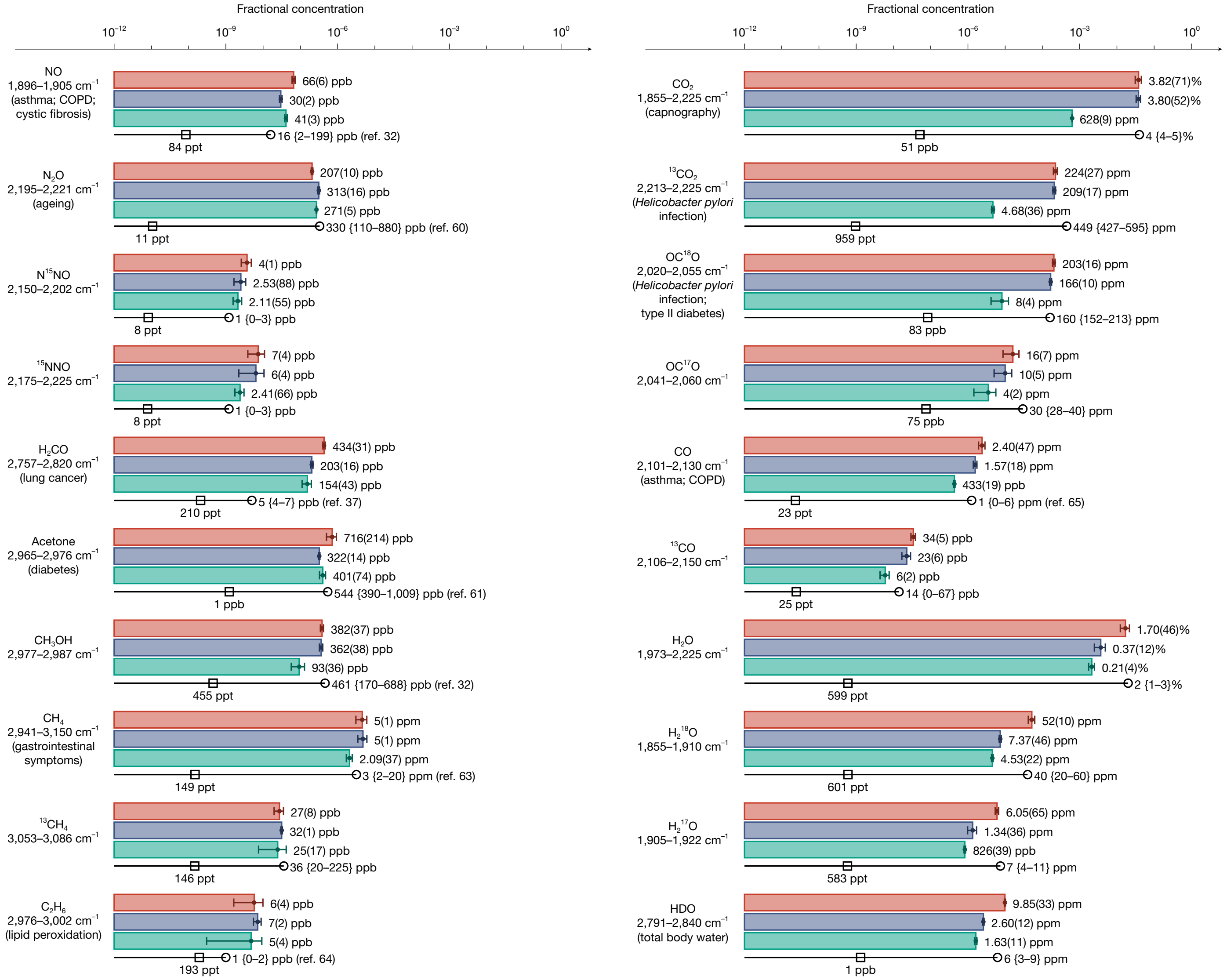

**Fig. 6 | Molecular concentrations summary.** Summary of a total of 20 species measured for nasal breath (red bars), oral breath (blue bars) and ambient air (green bars). For each species, its absorption feature wavenumber ranges, the fitted concentrations and standard deviation errors and known clinical relevance for breath analysis are given. On the stem lines, typical concentrations[32,37,60–65] found in exhaled breath are indicated with open circles (the numbers inside the curly brackets provide the range of concentrations), whereas experimental detection sensitivity limits are indicated with open squares. COPD, chronic obstructive pulmonary disease.

measured and stabilized to cavity resonances at high servo bandwidth[2,24,25]. Further, cavity swept lock permits the entire instantaneous comb bandwidth to be coupled through the cavity despite the presence of strong intracavity dispersion and it enables a large dynamic range for servo and robust sustentation against incidental mechanical jittering. These make the instrument much more practical and robust for out-of-laboratory operation and at much improved data-collection efficiency.

Finally, extending comb–cavity ringdown to over 1,000 cm$^{-1}$ mid-infrared spectral coverage is a new opportunity to simultaneously detect chemical compounds of various sizes. Molecular absorption spectra are robustly determined against a constant baseline determined by the reflectivity of the cavity mirrors. This provides exceptional versatility to the technique for demanding applications of measuring absorption features of arbitrary spectral widths. As evident from the presented results, rovibrational quantum-state-resolved absorption signals from small molecules with a characteristic spectral width of about 0.1–1.0 GHz (for example, nitric oxide) and state-unresolved signals from medium-sized molecules at roughly 10–100 cm$^{-1}$ (for example, acetone and methanol) are all robustly measured. This unique and outstanding capability paves the way to detect viruses[43] and proteins[44] that are potentially present in breath, in which absorption features span over 1,000 cm$^{-1}$. Direct quantification of viral loads in exhaled breath can allow differentiation of viral response from host response in diagnostic scenarios such as detection of SARS-CoV-2 infection to yield further mechanistic insights[3]. To verify the use of MRCI also for fundamental molecular spectroscopic studies[11], we demonstrate a measurement at comb-mode resolution to showcase its reliability for measuring molecular absorption lineshape (see Extended Data Fig. 6).

## Conclusions and outlook

Highly dispersive gas samples can now be extensively measured. The MRCI technique resolves the important gaps preventing promising trace-gas-sensing tools from further development and provides a robust prospect for wide-range deployment for real-world applications. MRCI enables: (1) weakest, strongest, sharpest and broadest absorption features to be measured simultaneously; (2) scalable improvement to both spectral coverage and cavity finesse without sacrificing spectral resolution; (3) comb sources operation under free-running condition and no requirement of high-bandwidth servo control; (4) robust, automatable and high-efficiency data collection at little to no trained expertise.

New practical possibilities are opened for the creation of large-scale breathomics databases for investigations of different health-related symptoms in parallel[26], as well as monitoring campaigns over numerous gaseous emissions for climate change from energy production[27], vehicles[28], soil microbes[29] and vegetation[30]. High-quality comb-based massive datasets generated for the 'odour' of gas samples will be integrated with machine-learning analysis tools[3] to facilitate more thorough investigations for science and new applications for industry. Free from chemical derivatization[45], instrument calibration and absorptions external to the enclosed cavity regions, MRCI promises enhanced accuracy, reproducibility and reduced labour for large-scale detection of chemical compounds of various sizes and of different isotopologue, isomer and isobar origins. MRCI can be broadly implemented, requiring minimum to no modification of existing experimental setups and can stimulate high-throughput mirror coating characterization[46] and molecular database construction, particularly for weakly absorbing large-sized molecules[11]. Comb sources produced with integrated photonics[18,47] may make use of the compatibility of MRCI with free-running combs to facilitate the construction of portable devices. When laser sources are constructed with simplicity and are robust to maintain working condition[20], dual-comb readout may prove to be advantageous over Michelson interferometry in practicality for implementing MRCI.

Last, MRCI is a massively multiplexed information-extraction methodology, in which channels of information encoded into the field intensity dynamics of frequency comb lines can be determined in parallel from its frequency domain equivalent carriers. The method can be generalized to measuring periodic dynamics of various kinds, for example, chemical kinetics[12]. To illustrate this, assume a chemical reaction is triggered in a repetitive manner with a repetition period commensurate with the reaction timescale. The chemical-reaction kinetics will be multiplied with the cavity ringdown dynamics in real time and their product can be determined through MRCI. Pre-measured empty cavity ringdown dynamics allows the chemical-reaction kinetics to be separated. Although the interferometry scan can potentially take much longer time than a single-shot reaction event, this process can be considered as signal averaging for better signal-to-noise ratio besides ensuring sufficient spectral resolution.

## Online content

Any methods, additional references, Nature Portfolio reporting summaries, source data, extended data, supplementary information, acknowledgements, peer review information; details of author contributions and competing interests; and statements of data and code availability are available at https://doi.org/10.1038/s41586-024-08534-2.

1. Thorpe, M. J., Balslev-Clausen, D., Kirchner, M. S. & Ye, J. Cavity-enhanced optical frequency comb spectroscopy: application to human breath analysis. *Opt. Express* **16**, 2387–2397 (2008).
2. Liang, Q. et al. Ultrasensitive multispecies spectroscopic breath analysis for real-time health monitoring and diagnostics. *Proc. Natl Acad. Sci.* **118**, e2105063118 (2021).
3. Liang, Q. et al. Breath analysis by ultra-sensitive broadband laser spectroscopy detects SARS-CoV-2 infection. *J. Breath Res.* **17**, 036001 (2023).
4. Rieker, G. B. et al. Frequency-comb-based remote sensing of greenhouse gases over kilometer air paths. *Optica* **1**, 290–298 (2014).
5. Herman, D. I. et al. Precise multispecies agricultural gas flux determined using broadband open-path dual-comb spectroscopy. *Sci. Adv.* **7**, eabe9765 (2021).
6. Giorgetta, F. R. et al. Open-path dual-comb spectroscopy for multispecies trace gas detection in the 4.5–5 μm spectral region. *Laser Photonics Rev.* **15**, 2000583 (2021).
7. Bui, T. Q. et al. Spectral analyses of *trans*- and *cis*-DOCO transients via comb spectroscopy. *Mol. Phys.* **116**, 3710–3717 (2018).
8. Changala, P. B., Spaun, B., Patterson, D., Doyle, J. M. & Ye, J. Sensitivity and resolution in frequency comb spectroscopy of buffer gas cooled polyatomic molecules. *Appl. Phys. B* **122**, 292 (2016).
9. Spaun, B. et al. Continuous probing of cold complex molecules with infrared frequency comb spectroscopy. *Nature* **533**, 517–520 (2016).
10. Foltynowicz, A., Maslowski, P., Fleisher, A. J., Bjork, B. J. & Ye, J. Cavity-enhanced optical frequency comb spectroscopy in the mid-infrared application to trace detection of hydrogen peroxide. *Appl. Phys. B* **110**, 163–175 (2013).
11. Changala, P. B., Weichman, M. L., Lee, K. F., Fermann, M. E. & Ye, J. Rovibrational quantum state resolution of the $C_{60}$ fullerene. *Science* **363**, 49–54 (2019).
12. Bjork, B. J. et al. Direct frequency comb measurement of OD + CO → DOCO kinetics. *Science* **354**, 444–448 (2016).
13. Bui, T. Q. et al. Direct measurements of DOCO isomers in the kinetics of OD + CO. *Sci. Adv.* **4**, eaao4777 (2018).
14. Fleisher, A. J. et al. Mid-infrared time-resolved frequency comb spectroscopy of transient free radicals. *J. Phys. Chem. Lett.* **5**, 2241–2246 (2014).
15. Lu, C., Morville, J., Rutkowski, L., Vieira, F. S. & Foltynowicz, A. Cavity-enhanced frequency comb vernier spectroscopy. *Photonics* **9**, 222 (2022).
16. Sulzer, P. et al. Cavity-enhanced field-resolved spectroscopy. *Nat. Photonics* **16**, 692–697 (2022).
17. Khodabakhsh, A. et al. Fourier transform and Vernier spectroscopy using an optical frequency comb at 3–5.4 μm. *Opt. Lett.* **41**, 2541–2544 (2016).
18. Sterczewski, L. A. et al. Cavity-enhanced Vernier spectroscopy with a chip-scale mid-infrared frequency comb. *ACS Photonics* **9**, 994–1001 (2022).
19. Haakestad, M. W., Lamour, T. P., Leindecker, N., Marandi, A. & Vodopyanov, K. L. Intracavity trace molecular detection with a broadband mid-IR frequency comb source. *J. Opt. Soc. Am. B* **30**, 631–640 (2013).
20. Markus, C. R. et al. Cavity-enhanced dual-comb spectroscopy in the molecular fingerprint region using free-running quantum cascade lasers. *J. Opt. Soc. Am. B* **41**, E56–E64 (2024).
21. Adler, F., Thorpe, M. J., Cossel, K. C. & Ye, J. Cavity-enhanced direct frequency comb spectroscopy: technology and applications. *Annu. Rev. Anal. Chem.* **3**, 175–205 (2010).
22. Thorpe, M. J., Moll, K. D., Jones, R. J., Safdi, B. & Ye, J. Broadband cavity ringdown spectroscopy for sensitive and rapid molecular detection. *Science* **311**, 1595–1599 (2006).
23. Okeefe, A. & Deacon, D. A. G. Cavity ring-down optical spectrometer for absorption-measurements using pulsed laser sources. *Rev. Sci. Instrum.* **59**, 2544–2551 (1988).
24. Lisak, D. et al. Dual-comb cavity ring-down spectroscopy. *Sci. Rep.* **12**, 2377 (2022).
25. Dubroeucq, R. & Rutkowski, L. Optical frequency comb Fourier transform cavity ring-down spectroscopy. *Opt. Express* **30**, 13594–13602 (2022).
26. Costello, B. D. et al. A review of the volatiles from the healthy human body. *J. Breath Res.* **8**, 014001 (2014).
27. Sherwin, E. D. et al. US oil and gas system emissions from nearly one million aerial site measurements. *Nature* **627**, 328–334 (2024).
28. Anenberg, S. C. et al. Impacts and mitigation of excess diesel-related NOx emissions in 11 major vehicle markets. *Nature* **545**, 467–471 (2017).
29. van Groenigen, K. J., Osenberg, C. W. & Hungate, B. A. Increased soil emissions of potent greenhouse gases under increased atmospheric $CO_2$. *Nature* **475**, 214–216 (2011).
30. Deshmukh, C. S. et al. Net greenhouse gas balance of fibre wood plantation on peat in Indonesia. *Nature* **616**, 740–746 (2023).
31. Adler, F. et al. Phase-stabilized, 1.5 W frequency comb at 2.8–4.8 μm. *Opt. Lett.* **34**, 1330–1332 (2009).
32. Dweik, R. A. et al. An official ATS clinical practice guideline: interpretation of exhaled nitric oxide levels ($FE_{NO}$) for clinical applications. *Am. J. Respir. Crit. Care Med.* **184**, 602–615 (2011).
33. Lundberg, J. O. N. et al. High nitric-oxide production in human paranasal sinuses. *Nat. Med.* **1**, 370–373 (1995).
34. Andersson, J. A., Uddman, R. & Cardell, L. O. Carbon monoxide is endogenously produced in the human nose and paranasal sinuses. *J Allergy Clin. Immunol.* **105**, 269–273 (2000).
35. Mitsui, T., Miyamura, M., Matsunami, A., Kitagawa, K. & Arai, N. Measuring nitrous oxide in exhaled air by gas chromatography and infrared photoacoustic spectrometry. *Clin. Chem.* **43**, 1993–1995 (1997).
36. Costello, B. P. J. D., Ledochowski, M. & Ratcliffe, N. M. The importance of methane breath testing: a review. *J. Breath Res.* **7**, 024001 (2013).
37. Wang, T. S., Pysanenko, A., Dryahina, K., Spanel, P. & Smith, D. Analysis of breath, exhaled via the mouth and nose, and the air in the oral cavity. *J. Breath Res.* **2**, 037013 (2008).
38. Smith, D. & Spanel, P. Pitfalls in the analysis of volatile breath biomarkers: suggested solutions and SIFT-MS quantification of single metabolites. *J. Breath Res.* **9**, 022001 (2015).
39. Nielsen, G. D. & Wolkoff, P. Cancer effects of formaldehyde: a proposal for an indoor air guideline value. *Arch. Toxicol.* **84**, 423–446 (2010).
40. Winkowski, M. & Stacewicz, T. Optical detection of formaldehyde in air in the 3.6 μm range. *Biomed. Opt. Express* **11**, 7019–7031 (2020).
41. Bernhardt, B. et al. Cavity-enhanced dual-comb spectroscopy. *Nat. Photonics* **4**, 55–57 (2010).
42. Foltynowicz, A., Ban, T., Maslowski, P., Adler, F. & Ye, J. Quantum-noise-limited optical frequency comb spectroscopy. *Phys. Rev. Lett.* **107**, 233002 (2011).
43. Xia, Q. et al. Single virus fingerprinting by widefield interferometric defocus-enhanced mid-infrared photothermal microscopy. *Nat. Commun.* **14**, 6655 (2023).
44. López-Lorente, A. I. & Mizaikoff, B. Mid-infrared spectroscopy for protein analysis: potential and challenges. *Anal. Bioanal. Chem.* **408**, 2875–2889 (2016).
45. Spanel, P. & Smith, D. Quantification of trace levels of the potential cancer biomarkers formaldehyde, acetaldehyde and propanol in breath by SIFT-MS. *J. Breath Res.* **2**, 046003 (2008).
46. Truong, G.-W. et al. Mid-infrared supermirrors with finesse exceeding 400 000. *Nat. Commun.* **14**, 7846 (2023).
47. Suh, M. G., Yang, Q. F., Yang, K. Y., Yi, X. & Vahala, K. J. Microresonator soliton dual-comb spectroscopy. *Science* **354**, 600–603 (2016).
48. Muraviev, A. V., Smolski, V. O., Loparo, Z. E. & Vodopyanov, K. L. Massively parallel sensing of trace molecules and their isotopologues with broadband subharmonic mid-infrared frequency combs. *Nat. Photonics* **12**, 209–214 (2018).

49. Tian, L. et al. Gas phase multicomponent detection and analysis combining broadband dual-frequency comb absorption spectroscopy and deep learning. *Commun. Eng.* **2**, 54 (2023).
50. Zhu, F. et al. Mid-infrared dual frequency comb spectroscopy based on fiber lasers for the detection of methane in ambient air. *Laser Phys. Lett.* **12**, 095701 (2015).
51. Johnson, T. A. & Diddams, S. A. Mid-infrared upconversion spectroscopy based on a Yb:fiber femtosecond laser. *Appl. Phys. B* **107**, 31–39 (2012).
52. Hjältén, A., Foltynowic, A. & Sadiek, I. Line positions and intensities of the v1 band of $^{12}CH_3I$ using mid-infrared optical frequency comb Fourier transform spectroscopy. *J. Quant. Spectrosc. Radiat. Transf.* **306**, 108646 (2023).
53. Zuo, Z. et al. Broadband mid-infrared molecular spectroscopy based on passive coherent optical-optical modulated frequency combs. *Photonics Res.* **9**, 1358–1368 (2021).
54. Tomaszewska-Rolla, D. et al. Mid-infrared optical frequency comb spectroscopy using an all-silica antiresonant hollow-core fiber. *Opt. Express* **32**, 10679–10689 (2024).
55. Adler, F. et al. Mid-infrared Fourier transform spectroscopy with a broadband frequency comb. *Opt. Express* **18**, 21861–21872 (2010).
56. Sterczewski, L. A. et al. Mid-infrared dual-comb spectroscopy with interband cascade lasers. *Opt. Lett.* **44**, 2113–2116 (2019).
57. Komagata, K. N., Wittwer, V. J., Südmeyer, T., Emmenegger, L. & Gianella, M. Absolute frequency referencing for swept dual-comb spectroscopy with midinfrared quantum cascade lasers. *Phys. Rev. Res.* **5**, 013047 (2023).
58. Hjältén, A. et al. Optical frequency comb Fourier transform spectroscopy of $^{14}N_2{}^{16}O$ at 7.8 µm. *J. Quant. Spectrosc. Radiat. Transf.* **271**, 107734 (2021).
59. Germann, M. et al. A methane line list with sub-MHz accuracy in the 1250 to 1380 $cm^{-1}$ range from optical frequency comb Fourier transform spectroscopy. *J. Quant. Spectrosc. Radiat. Transf.* **288**, 108252 (2022).
60. Dawson, B. et al. Measurements of methane and nitrous oxide in human breath and the development of UK scale emissions. *PLoS One* **18**, e0295157 (2023).
61. Wang, Z. N. & Wang, C. J. Is breath acetone a biomarker of diabetes? A historical review on breath acetone measurements. *J. Breath Res.* **7**, 037109 (2013).
62. Turner, C., Spanel, P. & Smith, D. A longitudinal study of methanol in the exhaled breath of 30 healthy volunteers using selected ion flow tube mass spectrometry, SIFT-MS. *Physiol. Meas.* **27**, 637–648 (2006).
63. Dryahina, K., Smith, D. & Spanel, P. Quantification of methane in humid air and exhaled breath using selected ion flow tube mass spectrometry. *Rapid Commun. Mass Spectrom.* **24**, 1296–1304 (2010).
64. Paredi, P., Kharitonov, S. A. & Barnes, P. J. Elevation of exhaled ethane concentration in asthma. *Am. J. Respir. Crit. Care Med.* **162**, 1450–1454 (2000).
65. Cunnington, A. J. & Hormbrey, P. Breath analysis to detect recent exposure to carbon monoxide. *Postgrad. Med. J.* **78**, 233–237 (2002).

# Methods

## Cavity swept lock on $f_{\mathrm{rep}}$, $f_{\mathrm{ceo}}$, FSR and intracavity dispersion

**$f_{\mathrm{rep}}$, $f_{\mathrm{ceo}}$ and FSR.** The shape of the cavity transmission bursts is dependent on the values of comb repetition rate ($f_{\mathrm{rep}}$), offset frequency ($f_{\mathrm{ceo}}$) and cavity free spectral range (FSR). A general scheme for implementing a cavity swept lock is presented in Extended Data Fig. 1. This scheme is used to fully stabilize all relevant frequencies ($f_{\mathrm{rep}}$, $f_{\mathrm{ceo}}$ and FSR) for our data collected at comb-mode resolution (Extended Data Fig. 6). For all data shown in the main text, in which data are all collected at modest instrument resolution ≥800 MHz, we engage only the servo using the odd-order Fourier components for locking the $f_{\mathrm{rep}}$–FSR detuning. This is because comb and cavity absolute frequencies change less than the magnitude of instrument resolution over the acquisition time of the interferogram. Further engaging the rest of the servos is thus not necessary.

**Intracavity dispersion.** Molecular absorption and mirror spectral response result in displacement of cavity resonance frequencies to mismatch from comb lines. To quantify, consider a cavity of length $L_{\mathrm{cav}}$, intracavity refractive index $n = 1 + \Delta n$ and phase delay per reflection from a cavity mirror surface $\Delta\phi$. The resonant condition requires the round-trip total phase delay to be integer multiples of 2π:

$$2kL_{\mathrm{cav}} + 2\Delta\phi = 2m\pi, \qquad (1)$$

equivalently,

$$\tilde{\nu} \times 2L_{\mathrm{cav}} + \Delta n \times \tilde{\nu} \times 2L_{\mathrm{cav}} + \Delta\phi/\pi = m, \qquad (2)$$

in which $k = 2\pi(1+\Delta n)\tilde{\nu}$ is the wavevector, $\tilde{\nu}$ is the wavenumber and $m$ is an integer called the mode index. From cavity finesse $F$ defined as the ratio of cavity FSR to cavity resonance width, comb walks off from cavity resonances when the molecular dispersion term $\Delta n \times \tilde{\nu} \times 2L_{\mathrm{cav}}$ or the mirror dispersion term $\Delta\phi/\pi$ in equation (2) exceeds that corresponding to changing $m$ by $1/F$. To illustrate, consider the measurement of an ambient air sample over 2,700–3,330 cm$^{-1}$. Dispersion is estimated at $\Delta n \geq 4 \times 10^{-7}$ and $\Delta\phi \geq 50°$ (Extended Data Fig. 2). Take $\tilde{\nu} = 3{,}000\ \mathrm{cm}^{-1}$ and $L_{\mathrm{cav}} = 50$ cm. Molecular dispersion contributes $\Delta n \times \tilde{\nu} \times 2L_{\mathrm{cav}} = 0.12$. Displacement in cavity resonance frequencies from molecular dispersion alone thus amounts to 12% of the cavity FSR and 120 times the cavity resonance width, if finesse $F = 1{,}000$. A transient coupling scheme should be used to replace tight comb–cavity coupling. Extended Data Fig. 2 provides further details on strategies for cavity swept lock engagement in the presence of strong dispersion.

## MRCI

**Theoretical model.** Consider a high-finesse cavity made of two identical cavity mirrors that is coupled with a passively stable frequency comb. The cavity length is modulated by a sinusoidal wave at rate $\omega_m$ centred at the cavity length of $d_0$. The mean cavity FSR is matched to the comb spacing. The cavity resonance frequency modulation depth is smaller than the comb spacing but large enough to permit the instantaneous comb bandwidth to resonant couple through the cavity twice per modulation period: once when the cavity length is swept up and the other when it is swept down. For simplicity, imagine for now that the incident comb is shut off during the cavity length downsweep (more discussion later). Transmission bursts from all cavity resonances thus have the same time periodicity $T = 2\pi/\omega_m$ and emitted all from the cavity upsweep. The electric field intensity components $|E_{\mathrm{cav},i}(t)|^2$ in time $t$ from the $i$th cavity resonance can be decomposed into a Fourier series:

$$|E_{\mathrm{cav},i}(t)|^2 = \sum_{n=-\infty}^{+\infty} f_{ni} \exp(\mathrm{j}n\omega_m t), \qquad (3)$$

in which $f_{ni}$ is the $n$th Fourier component from the $i$th resonance and j denotes the imaginary unit.

The Michelson interferometer introduces a modulation to the field intensity profile that is specific to the optical frequency. The laser intensity versus time readout by the photodetectors in the Michelson interferometer is expressed as $\Sigma_i|E_{\mathrm{cav},i}(t)|^2[1 \pm \cos(\omega_i t)]$, in which $\omega_i = k_i v$ is the Doppler frequency shift, $k_i$ is the optical wavenumber and $v$ is the optical path length difference (OPD) scanning speed assumed to be a constant (more discussion later). The signal carriers are spectrally detected at RF frequencies over $|n\omega_m \pm \omega_i|$ and the non-cosine-modulated terms at $|n|\omega_m$. They are spectrally isolated if $\omega_i$ for all $i$ are non-equal to integer multiples of $\omega_m/2$. The acquisition time per interferogram should be sufficiently long to resolve different RF components. Spectral intensities measured by the non-cosine-modulated terms can be used to determine the relative response function of photodetectors to implement digital autobalancing. The balanced intensity output $I(t)$ after cancelling out the non-cosine-modulated terms is given by:

$$I(t) = 2\sum_i \sum_{n=-\infty}^{+\infty} f_{ni} \exp(\mathrm{j}n\omega_m t)\cos(\omega_i t). \qquad (4)$$

The expression of $|E_{\mathrm{cav},i}(t)|^2$ for a single transmission burst (that is, cavity resonance swept through a comb line once) has previously been derived in ref. 66. Omitting common proportionality and assuming $T \gg \tau_{\mathrm{RD},i}$, $f_{ni}$ can be calculated from:

$$f_{ni} = \int_{-\infty}^{\infty} \exp\left(-\frac{t'}{\tau_{\mathrm{RD},i}}\right) |\mathrm{erfc}[\Lambda_i(t')]|^2 \exp(-\mathrm{j}n\omega_m t')\mathrm{d}t', \qquad (5)$$

in which $\tau_{\mathrm{RD},i} = \tau/(-2\ln\rho_i)$ is the cavity ringdown time, $\tau = 2d_0/c$ the cavity round-trip time, $c$ the speed of light, $\rho_i = r_i^2\exp[-(\alpha_i/2)\cdot 2d_0]$ the round-trip field loss, $r_i$ the mirror reflection coefficient, $\alpha_i$ the intracavity absorption coefficient and erfc the complementary error function. The $\Lambda_i(t')$ is given by

$$\Lambda_i(t') = \frac{1-j}{2\sqrt{2}}\left(\frac{1}{k_i v_i^{\mathrm{cav}}\tau}\right)^{1/2} \times (-\ln\rho_i) - \frac{1+j}{2\sqrt{2}}\left(\frac{1}{k_i v_i^{\mathrm{cav}}\tau}\right)^{1/2} \times 2k_i v_i^{\mathrm{cav}} t', \qquad (6)$$

in which $v_i^{\mathrm{cav}}$ is the cavity length swept velocity when the $i$th resonance is scanned to the comb line.

Equation (5) is used to fit the experimental data for $|f_{ni}|$ at the same $i$ over different $n$ to find $\tau_{\mathrm{RD},i}$. For molecular spectroscopy with the goal to determine $\alpha_i$, we compared the ringdown times measured with the cavity loaded ($\alpha_i \neq 0$) and unloaded ($\alpha_i = 0$) with a gas sample. From the dependence of $\tau_{\mathrm{RD},i}$ on $\rho_i$, $\alpha_i$ can be obtained from:

$$\alpha_i = \frac{1}{c}\left[\frac{1}{\tau_{\mathrm{RD},i}(\alpha_i \neq 0)} - \frac{1}{\tau_{\mathrm{RD},i}(\alpha_i = 0)}\right]. \qquad (7)$$

**Experimental implementation.** The MRCI technique was implemented in our experiment with the incident comb power passively staying on, a high-finesse cavity swept locked to the incident comb lines and a passively scanning Michelson interferometer. The $\omega_m$ and $\omega_i$ are not perfectly coherent. Below we detail their sources of incoherence and present our data-analysis strategies. These strategies are the key to removing the experimental needs to ensure perfect coherence in $\omega_m$ and $\omega_i$ that can require greatly increased experimental complexity and decreased robustness. A detailed workflow of the entire data-processing workflow is presented in Extended Data Fig. 3 and can be used as a reference for the rest of this section.

1. The $\omega_m$: owing to the presence of intracavity dispersion and piezo hysteresis, comb lines on cavity resonance at an earlier time during the cavity length upsweep are on resonance at a later time during the cavity downsweep. Although two transmission bursts are emitted

from each resonance per cavity length round-trip modulation period $T$, intensity component $|E_{\mathrm{cav},i}(t)|^2$ generally repeats at periodicity $T$ rather than $T/2$: the base pattern in repetition is that from a cavity upsweep and subsequent downsweeps. For equation (5) to be directly applicable, we process the transmission bursts from the upsweep separately from the downsweep. A logical TTL function phase-synchronized with the cavity modulation signals is digitally generated in the data post-processing to pick up transmission bursts solely from the upsweep (or downsweep) by means of multiplication to the raw interferogram data. This is equivalent to having the incident comb source shut off during the downsweep (or upsweep). The two sets of interferograms, one containing only the upsweep bursts and the other only the downsweep bursts, are processed separately by equation (5). On a separate note, when it is of interest to implement dispersion spectroscopy[67], the interferogram can be processed without separating the up and down bursts. Equation (5) would need to be modified to account for an emission time delay between adjacent up and down bursts from the expected time separation at $T/2$.

2. The $\omega_i$: conventional delay stage introduces considerable mechanical jitters, causing $\omega_i$ to fluctuate in time. The jittering of $\omega_i$ is small compared with the value of $\omega_m$ but must be properly accounted for in the data processing for applications at high spectral resolution. Equation (4) should be modified into a more general form by replacing $\omega_i t$ with $k_i z$:

$$I(t,z) = 2\sum_i \sum_{n=-\infty}^{+\infty} f_{ni}\exp(\mathrm{j}n\omega_m t)\cos(k_i z). \tag{8}$$

Here $z$ is the OPD scanned. In the experiment, the real-time mapping from $z$ to $t$ can be measured with a wavelength-stable continuous-wave laser co-propagating with the comb light into the Michelson interferometer. With both the interferogram $I(t,z)$ and space variable $z$ sampled by the same time array, the explicit dependence of the interferogram on time can be removed using demodulation: first, we multiply the interferogram with digitally generated $\exp(-\mathrm{j}n'\omega_m t)$ sampled over the same time array, then bandpass the Doppler frequency shifts $\{\omega_i\}$. This results in

$$\{I(t,z)\times\exp(-\mathrm{j}n'\omega_m t)\}_{\mathrm{bandpass}} = 2\sum_i f_{n'i}\cos(k_i z). \tag{9}$$

The demodulated output is a complex function of a single variable $z$ and can be non-uniformly Fourier transformed to find the spectrum of $|f_{n'i}|$ versus $k_i$. The value of $|f_{n'i}|$ for all $i$ can thus be determined. The demodulation is repeated at different $n'$ spanning negative to positive integers: the $|f_{n'i}|$ and $|f_{-n'i}|$ are independently measured by two signal carriers at $n'\omega_m + \omega_i$ and $n'\omega_m - \omega_i$ but probe the same physical quantity $|f_{n'i}| = |f_{-n'i}|$ (see equation (5)). They can be averaged together to improve the signal-to-noise ratio.

To summarize, the raw interferogram is first linearly decomposed into two interferograms: one contains bursts exclusively from the upsweep and the other contains bursts exclusively from the downsweep. The two interferograms are respectively processed to find $|f_{ni}|$ containing non-negative $n$ using the demodulation technique. The two sets of $|f_{ni}|$ are averaged together and equation (5) is applied to find the ringdown time $\tau_{\mathrm{RD},i}$.

## Apparatus

**Frequency combs.** The comb used for the data collection in the 2,700–3,330-cm$^{-1}$ spectral range is a singly resonant OPO built from a periodically poled lithium niobate crystal and synchronously pumped by an ytterbium comb at 137 MHz repetition rate centred at 1,064 nm and with a pulse duration of 100 fs. This OPO is previously reported in ref. 31. The instantaneous bandwidth is 180 cm$^{-1}$. Spectral tuning is performed by translating the crystal location. The comb used for the 1,850–2,230 cm$^{-1}$ spectral range is built from a new singly resonant OPO using a zinc germanium phosphide crystal synchronously pumped by a thulium comb at 110 MHz repetition rate centred at 1,960 nm and with a pulse duration of 1,000 fs. This comb source was developed to overcome the difficulty of oxides materials generating sufficient power per comb tooth at ≥4.8 μm wavelength necessary for cavity-enhanced spectrosocpy[17,68]. The OPO is designed following the strategy previously documented in ref. 69. Both the spatial walk-off from birefringence and the temporal walk-off from group velocity mismatch are taken into account to design the threshold pump power to be sufficiently small compared with the maximum available pump power. Ring cavity geometry rather than linear geometry is adopted to avoid round-trip signal absorption loss from one more pass through the crystal. The cavity is unpurged but sealed for passive frequency stability. The OPO had an instantaneous bandwidth of 60 cm$^{-1}$ and is broadly tunable in the range 1,850–2,230 cm$^{-1}$ simply by translating the OPO cavity length to manipulate the group delay dispersion. Limited power below 1,850 cm$^{-1}$ is because of water absorption and above 2,230 cm$^{-1}$ because of carbon dioxide absorption. When the idler is tuned to 2,040 cm$^{-1}$ (4.9 μm), power per comb tooth up to 13 μW is measured. This is more than a factor of ten higher than all comb sources ever reported near the 5 μm wavelength[48,70–74]. For further details about the OPO, see Extended Data Fig. 5.

**Data acquisition.** High-reflectivity mirrors for both cavities were purchased from LohnStar Optics (technical communication only; not endorsement). Both cavities have their mean FSR matched to twice the frequency spacing of the incident combs. The 5-μm cavity is 68 cm in length and modulated at 13 kHz. The 3-μm cavity is 55 cm in length and modulated at 18 kHz. The modulation rates are set low enough to enable sufficient time for each ringdown event to eventually decay down to the detector noise floor. The modulation rate is higher for the 3-μm cavity owing to smaller cavity ringdown times overall. Servo error signals generated from the photodetectors in the Michelson interferometer are summed and demodulated at the third harmonics of the modulation frequencies for feedback stabilization of the cavity lengths to the comb line frequencies. Further servo details apply to our data collected at comb-mode resolution presented in Extended Data Fig. 6. For details, see the section ‘Cavity swept lock on $f_{\mathrm{rep}}$, $f_{\mathrm{ceo}}$, FSR and intracavity dispersion’. The OPO spectral centre and the OPD scanning speed of the interferometer are feedforward adjusted automatically. The feedforward map ensures that every interferogram scan is executed such that the Doppler frequency shifts stay about the same and are sufficiently detuned from integer multiples of half the cavity length modulation rates to avoid spectral overlapping issues. For each scan, the OPD scanning speed is fixed at no faster than 200 mm s$^{-1}$. A total of three data channels low passed at 1 MHz are collected simultaneously at 2-Msps sampling rate and 16-bit resolution: interference fringes for the comb light using two photodetectors and for the continuous-wave laser with one photodetector. No photodetectors require cooling by liquid nitrogen. Data collection for the entire 5-μm spectral range (1,850–2,230 cm$^{-1}$) is fully automated, with servo loops robustly sustained. For the 3-μm range (2,700–3,330 cm$^{-1}$), however, the picomotor actuator used for adjusting the crystal location introduces considerable mechanical jitter that occasionally disengages the servo. We expect that future upgrades to crystal positioning and/or implementing automatic servo re-engagement can fully automate data collection also for the 3-μm region. Breath and air data are processed at 800 MHz instrument resolution and the acquisition time per interferogram is about 2 s. Full survey spectrum for the 5-μm spectral range at 380 cm$^{-1}$ coverage is collected with about 500 interferograms, whereas roughly 1,400 interferograms were required for the 3-μm range at 630 cm$^{-1}$ coverage. Empty cavity survey data were collected at 2 GHz instrument resolution. For all experimental data, the demodulation was performed for the 5-μm data up to the 20th Fourier harmonics and for the 3-μm data up to the 15th harmonics. This used signal carriers measured with high signal-to-noise ratio up to 300 kHz electronic bandwidth. Fourier harmonics spectra collected at different spectroscopic regions were summed before determining the full coverage ringdown spectrum. We carried out data analysis using a 32-core 3975WX CPU and an RTX A6000 GPU. The GPU was used for accelerating demodulation and Fourier transforms. The multicore CPU was used for accelerating ringdown extraction. Example interferogram data are presented in Extended Data Fig. 4.

### Detection sensitivity

Fourier transform spectroscopy relates spectral intensity signal-to-noise ratio $(\mathrm{S/N})_\mathrm{f}$ to time domain interferogram intensity signal-to-noise ratio $(\mathrm{S/N})_\mathrm{t}$ based on[42,75]

$$(\mathrm{S/N})_\mathrm{f} = \frac{\sqrt{K}}{M_\mathrm{tot}} \times (\mathrm{S/N})_\mathrm{t}, \qquad (10)$$

in which $K$ is the number of data points in the interferogram and $M_\mathrm{tot}$ is the total number of spectral elements. Suppose a periodic time dynamics measured by interferometry can be decomposed into a list of Fourier harmonics with non-negligible intensity up to the harmonics order of $n_\mathrm{max}$. The absorption feature at each optical frequency is thus measured by a total of $2n_\mathrm{max} + 1$ spectral elements (from $-n_\mathrm{max}$ to $n_\mathrm{max}$). Thus $M_\mathrm{tot} = M \cdot (2n_\mathrm{max} + 1)$, in which $M$ is the number of spectral elements per Fourier harmonics. $M$ is equal to the instantaneous comb coverage divided by the instrument resolution.

The spectral intensity noise-to-signal ratio $(\mathrm{N/S})_\mathrm{f} = \alpha_\mathrm{min} L_\mathrm{eff} \times \sqrt{2n_\mathrm{max}+1}$, in which $\alpha_\mathrm{min}$ is the MDA coefficient, $L_\mathrm{eff}$ is the light-molecule effective absorption path length and the $\sqrt{2n_\mathrm{max}+1}$ term accounts for noise reduction owing to repetitive measurements totalling $2n_\mathrm{max} + 1$ times. Thus,

$$\alpha_\mathrm{min} = (\mathrm{N/S})_\mathrm{t} \times \frac{M}{\sqrt{K}} \times \sqrt{2n_\mathrm{max}+1} \times \frac{1}{L_\mathrm{eff}} \qquad (11)$$

determines MDA at a given $(\mathrm{N/S})_\mathrm{t}$. At the shot noise limit, $(\mathrm{N/S})_\mathrm{t} = \sqrt{2eB/\eta P}$ and equation (11) recovers to the form previously derived in ref. 42 ($B$ the electronic bandwidth, $\eta$ the detector responsivity and $P$ the power incident on the detector). Using interferometry for measuring laser fields periodic in time ($n_\mathrm{max} \neq 0$) rather than static ($n_\mathrm{max} = 0$) results in a penalty in raising $\alpha_\mathrm{min}$ by a factor of $\sqrt{2n_\mathrm{max}+1}$.

For our apparatus, MDA at 1 s experimentally measured for the 3-μm (or 5-μm) region is $2.8 \times 10^{-7}\ \mathrm{cm}^{-1}\ \mathrm{Hz}^{-1/2}$ (or $7.8 \times 10^{-8}\ \mathrm{cm}^{-1}\ \mathrm{Hz}^{-1/2}$). Instrument resolution is 800 MHz and acquisition time per interferogram is 2 s. The measurements are conducted at base pressure (<3 mTorr) to minimize influence from molecular absorptions. Multi-element detection sensitivity for each molecular species was analysed from MDA at 1 s following the same analysis protocol detailed in ref. 2. Using $M = 6{,}750$ (or 2,250) and $n_\mathrm{max} = 15$ (or 20), we find $\alpha_\mathrm{min}\sqrt{T/M_\mathrm{tot}} = 6 \times 10^{-10}\ \mathrm{cm}^{-1}\ \mathrm{Hz}^{-1/2}$ (or $3 \times 10^{-10}\ \mathrm{cm}^{-1}\ \mathrm{Hz}^{-1/2}$) and $\alpha_\mathrm{min}\sqrt{T/M} = 3 \times 10^{-9}\ \mathrm{cm}^{-1}\ \mathrm{Hz}^{-1/2}$ (or $2 \times 10^{-9}\ \mathrm{cm}^{-1}\ \mathrm{Hz}^{-1/2}$).

### Sample collections and handling

This study was approved by the Institutional Review Board of the University of Colorado Boulder with protocol number 23-0536. Potential participants needed to be more than 18 years old to participate. There were no exclusion criteria. A participant was recruited from flyers. After written informed consent was obtained, the participant was contacted by a research member through emails for the scheduling of appointment time for breath samples collection. Just before sample collection, participants filled in an online questionnaire for the collection of demographics information and basic medical history. All information collected from the participant was stored and managed electronically through REDCap[76,77], a secure server for human research data management. All data exported from REDCap are de-identified. A study ID is used for correlating the questionnaire information with the breath analysis measurement results. The participant was advised to refrain from the consumption of food or drink (water excluded) and use of mouthwash or cough drops 1 h before providing breath samples. Two breath samples were collected: one by inhaling and exhaling through the nose but with the mouth closed (that is, nasal breath sample) and the other by inhaling and exhaling through the mouth but with the nose closed (that is, oral breath sample). The two samples were collected immediately after each other, both by inhaling to full lung capacity and followed by exhaling only the end-tidal breath into a Tedlar bag. The ambient air sample was collected on a separate day and also using a Tedlar bag. All collected gas samples were analysed immediately on the day of their collection. Used Tedlar bags were securely autoclaved and discarded. The chamber and cavity mirrors were flushed with ultra-high-purity argon gas at 4 l min$^{-1}$ for 10 min after each sample analysis to prevent potential cross-sample contamination. No degradation was observed for the cavity finesse.

### Molecular line fitting

The HITRAN database (edition 2020)[78] was used to extract concentrations totalling 20 molecular species. Methanol (214.2 K, 102.7 Torr) and acetone (209.8 K, 109.6 Torr) used cross-sectional data directly measured at specific temperature and pressure owing to the lack of line intensity data. For the other 18 species, cross-sectional data were calculated from the line intensity data using the Voigt profile evaluated at our experimental conditions (293.15 K, 100 Torr). Pressure broadening by air is considered, whereas self-pressure broadening and pressure shift of the line frequency centres were ignored. Molecular line fitting was performed bearing in mind that:

1. We may not be fitting all species that were detected, which could partly be attributed to lack of cross-sectional data. For exhaled breath, more than 1,000 species have been reported and more than 40% are hydrocarbons that can be spectroscopically detected in the 3–4-μm wavelength range[26,79]. Unfitted species that are potentially present in our experimental data are generally large molecules exhibiting state-unresolved ultra-broadband absorption features.
2. Strongly absorbing species such as water and carbon dioxide produced saturated absorption features. Errors in the prediction of absorption lineshape at far-off line centres[78] prohibits strongly absorbing species to have their concentrations determined over their saturated absorption regions. Further, other species that are weakly absorbing could also be affected when their line centres spectrally overlap with the saturated absorption features.

We have thus developed the following fitting strategy: we implemented a sliding window to select out 10 cm$^{-1}$ spectral range at a time for molecular line fitting. The window was step incremented at 0.5 cm$^{-1}$ to uniformly sample the whole coverage (1,010 cm$^{-1}$). Least squares fitting was performed with residuals given by the difference in the logarithm of absorption spectra. After fitting all windows separately, a slowly varying baseline was introduced for the whole coverage to vertically offset the simulated data to better match the experimental data. Here the baseline is to mimic the absorption features from unknown species and correct mispredicted absorption lineshape from the fitted species, both assumed to have a bandwidth broader than the window width at 10 cm$^{-1}$. With its introduction, the fittable species can be determined at minimized influence from these broadband features. We refit the spectrum with the simulated data added to the baseline in each window to compare it with the experimental data. After all windows were fitted, the baseline was updated again. The whole process was iterated five times for convergence. Fitted concentrations from the final iteration run were used for determining molecular concentrations. For each species, its concentration was determined from windows in which it can be reliably fitted. For the two saturated species $CO_2$ and $H_2O$, windows in which their maximum absorption coefficient exceeded $10^{-4}$ cm$^{-1}$ were discarded from statistical evaluations. For the other 18 species, only windows in which their maximum absorption cross-sections were within 70% of their strongest absorption cross-section in the whole coverage were considered. The cutoff percentage was chosen to be sufficiently low so that each species has its concentration evaluated generally from more than 30 windows for convergence. For each window, the averaging weight is given by its maximum absorption cross-section. Weighted mean and error were determined for each species over its considered windows. The selected window ranges for each of the 20 species are reported in Fig. 6.

## Data availability

All data and supporting materials have been deposited to Zenodo and can be accessed at https://doi.org/10.5281/zenodo.14254339 (ref. 80).

66. Poirson, J., Bretenaker, F., Vallet, M. & LeFloch, A. Analytical and experimental study of ringing effects in a Fabry–Perot cavity. Application to the measurement of high finesses. *J. Opt. Soc. Am. B* **14**, 2811–2817 (1997).
67. Wysocki, G. & Weidmann, D. Molecular dispersion spectroscopy for chemical sensing using chirped mid-infrared quantum cascade laser. *Opt. Express* **18**, 26123–26140 (2010).
68. Schunemann, P. G., Zawilski, K. T., Pomeranz, L. A., Creeden, D. J. & Budni, P. A. Advances in nonlinear optical crystals for mid-infrared coherent sources. *J. Opt. Soc. Am. B* **33**, D36–D43 (2016).
69. Iwakuni, K. et al. Phase-stabilized 100 mW frequency comb near 10 μm. *Appl. Phys. B* **124**, 128 (2018).
70. Vasilyev, S. et al. Longwave infrared (6.6–11.4 μm) dual-comb spectroscopy with 240,000 comb-mode-resolved data points at video rate. *Opt. Lett.* **48**, 2273–2276 (2023).
71. Smolski, V. et al. Half-Watt average power femtosecond source spanning 3–8 μm based on subharmonic generation in GaAs. *Appl. Phys. B* **124**, 101 (2018).
72. Heckl, O. H. et al. Three-photon absorption in optical parametric oscillators based on OP-GaAs. *Opt. Lett.* **41**, 5405–5408 (2016).
73. Leindecker, N. et al. Octave-spanning ultrafast OPO with 2.6-6.1μm instantaneous bandwidth pumped by femtosecond Tm-fiber laser. *Opt. Express* **20**, 7046–7053 (2012).
74. Vodopyanov, K. L., Sorokin, E., Sorokina, I. T. & Schunemann, P. G. Mid-IR frequency comb source spanning 4.4–5.4 μm based on subharmonic GaAs optical parametric oscillator. *Opt. Lett.* **36**, 2275–2277 (2011).
75. Newbury, N. R., Coddington, I. & Swann, W. Sensitivity of coherent dual-comb spectroscopy. *Opt. Express* **18**, 7929–7945 (2010).
76. Harris, P. A. et al. Research electronic data capture (REDCap)—a metadata-driven methodology and workflow process for providing translational research informatics support. *J. Biomed. Inform.* **42**, 377–381 (2009).
77. Harris, P. A. et al. The REDCap consortium: building an international community of software platform partners. *J. Biomed. Inform.* **95**, 103208 (2019).
78. Gordon, I. E. et al. The HITRAN2020 molecular spectroscopic database. *J. Quant. Spectrosc. Radiat. Transf.* **277**, 107949 (2022).
79. Drabinska, N. et al. A literature survey of all volatiles from healthy human breath and bodily fluids: the human volatilome. *J. Breath Res.* **15**, 034001 (2021).
80. Liang, Q., Bisht, A., Scheck, A., Schunemann, P. G. & Ye. J. Data for modulated ringdown comb interferometry for sensing of highly complex gases. *Zenodo* https://doi.org/10.5281/zenodo.14254339 (2025).

**Acknowledgements** We thank G. B. Rieker, S. A. Diddams, T. Q. Bui, O. H. Heckl, A. J. Fleisher, P. B. Changala and D. J. Nesbitt for helpful discussions. This work is supported by AFOSR FA9550-19-1-0148, NIST, NSF QLCI OMA–2016244 and NSF PHY-2317149.

**Author contributions** All authors contributed to the manuscript writing and results interpretation. Q.L. and J.Y. conceived the modulated ringdown comb interferometry technique. Q.L., A.B. and A.S. designed and constructed the spectroscopy setup and collected and analysed the spectroscopy data. The 5-μm optical parametric oscillator comb was designed and constructed by Q.L. using the zinc germanium phosphide nonlinear optical crystal provided by P.G.S. The research work was supervised by J.Y.

**Competing interests** A patent has been submitted for the technique of modulated ringdown comb interferometry by Q.L. and J.Y., both affiliated with JILA. The other authors declare no competing interests.

**Additional information**

**Correspondence and requests for materials** should be addressed to Qizhong Liang or Jun Ye.

**Peer review information** *Nature* thanks the anonymous reviewers for their contribution to the peer review of this work.

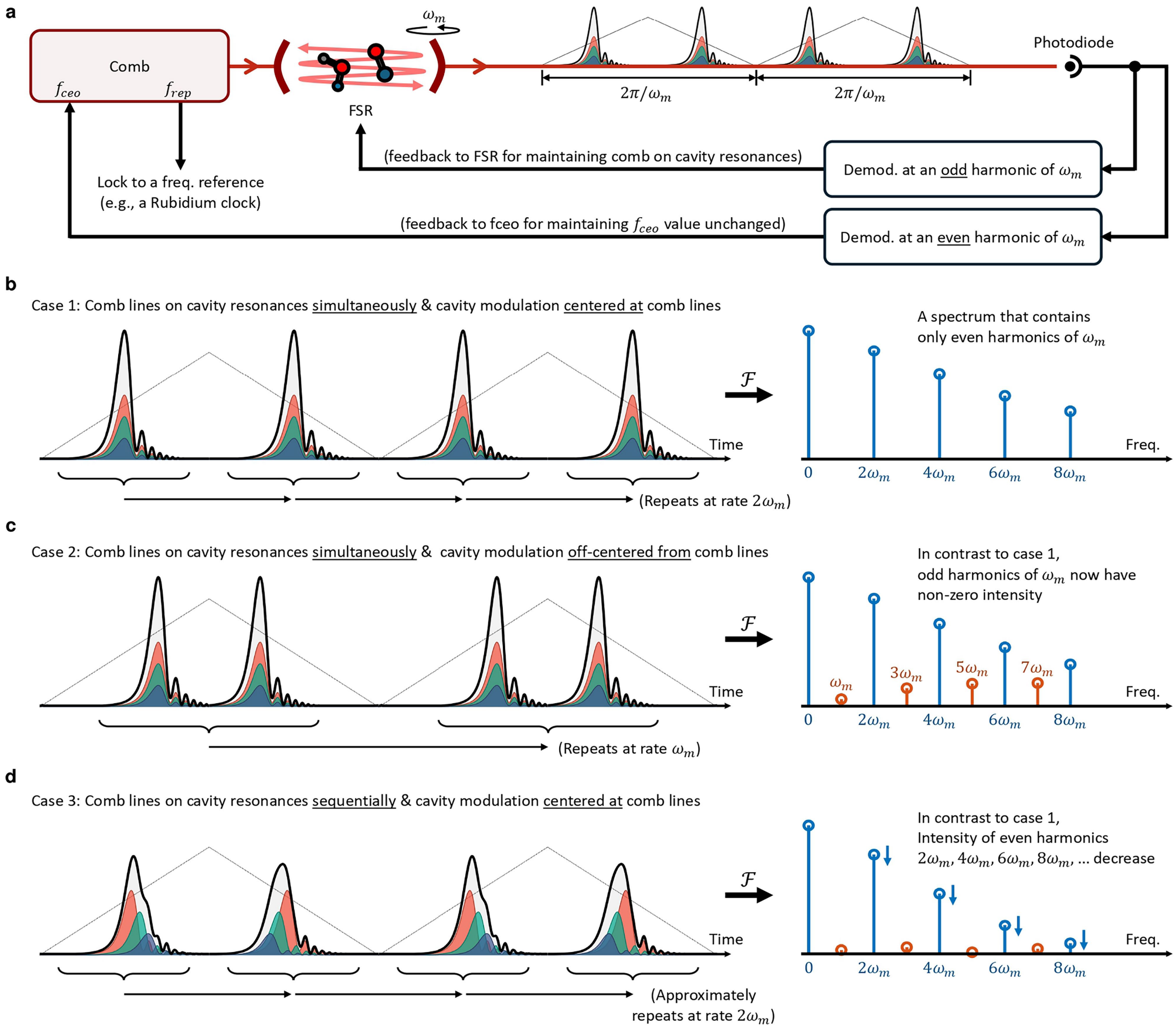

**Extended Data Fig. 1 | Cavity swept lock on comb-cavity frequency detuning.** For this figure, intracavity dispersion from molecules and mirrors and piezo hysteresis associated with the cavity length modulation are omitted for ease of discussion. **a**, Servo schematic. Error signals generated from demodulating the observed cavity transmission bursts at the even and odd harmonics of the cavity length modulation frequency $\omega_m$ are used for ensuring that comb frequencies ($f_{\text{rep}}$ and $f_{\text{ceo}}$) and cavity FSR can all be precisely stabilized to each other. Through further locking the $f_{\text{rep}}$ to an external frequency reference, the absolute frequencies for $f_{\text{rep}}$, $f_{\text{ceo}}$ and FSR can be fixed. To explain why the transmission bursts can be demodulated at even or odd harmonics of $\omega_m$ for respectively locking either $f_{\text{rep}}$–FSR frequency detuning or absolute frequency drift in $f_{\text{ceo}}$, consider three different cases shown in **b**–**d**. The triangle waves in dotted lines represent the cavity length periodic sweep. Red, green and blue curves represent transmission bursts generated from three different comb lines. Thick black curve takes the sum of the three comb signals and represents the time-dependent signal measured by a photodiode placed at the cavity transmission side. For each case, the intensity spectrum from Fourier transform of the black curve time signal is shown to the right. Comparing **b** with **c**, when $f_{\text{rep}}$–FSR frequency detuning is non-zero, the black curve observed from one consecutive cavity upsweep and downsweep form a base pattern repeating at rate $\omega_m$. This leads to non-zero intensity measured at odd harmonics of $\omega_m$. Comparing **b** with **d**, the slow drift in $f_{\text{ceo}}$ can result in comb lines appearing on cavity resonances sequentially. The black curve becomes wider in shape and its Fourier decomposition requires less intense high-frequency components. Thus, the even harmonics decrease in intensity (excluding the zeroth order, which will not change).

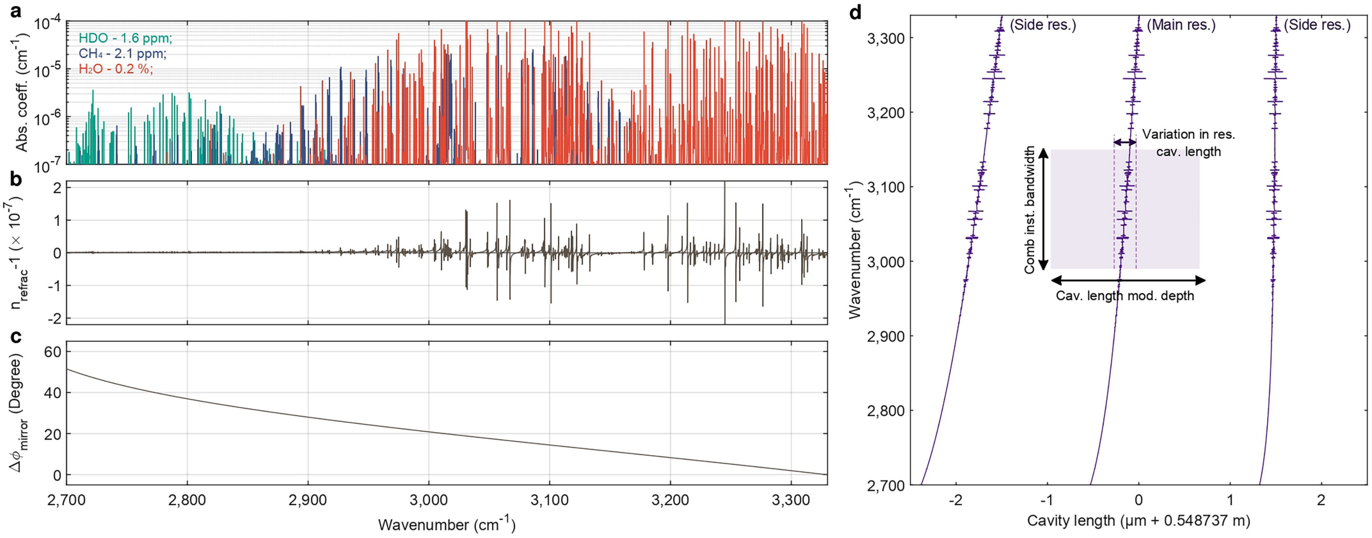

**Extended Data Fig. 2 | Cavity swept lock on molecular and mirror dispersion.** **a**, A simulation of ambient air absorption spectrum over 2,700–3,330 cm$^{-1}$, considering only the three most intense absorbers, HDO, $CH_4$ and $H_2O$, at concentrations of 1.6 ppm, 2.1 ppm and 0.2%, respectively, matched to our measured data presented in the main text. **b**, The corresponding intracavity refractive index spectrum calculated from **a** based on the Kramers–Kronig relations. It is non-rigorously assumed that molecular absorption is zero outside the plotted spectral range. Variation in the refractive index of more than $4 \times 10^{-7}$ can be seen. **c**, Phase delay per reflection from a mirror surface. The data are obtained from the vendor for the 3-µm cavity used in this work. We arbitrarily vertically offset the entire curve by a constant so that the phase delay is zero at the rightmost wavenumber (3,330 cm$^{-1}$). **d**, Cavity resonance frequency distribution calculated on the basis of the molecular dispersion data in **b** and mirror dispersion data in **c**, using equation (2) shown in Methods. For our comb-cavity main resonance at cavity length equal to 0.548737 m, which allows all comb lines on cavity resonance simultaneously if intracavity dispersion is absent, detuning the cavity length by about $\lambda/2$ allows one to go to the side resonance, in which $\lambda$ is the laser wavelength. Owing to the presence of intracavity dispersion, neither the main nor the side cavity resonances are a vertical straight line that will allow the comb instantaneous bandwidth to be coupled into the cavity simultaneously. In our presented data, molecular dispersion spreads the resonance cavity length either left or right every time a strong absorption line is scanned across, whereas mirror dispersion shifts the resonance cavity length to the left, which is slowly increasing with the decrease in wavenumber. At this level of dispersion, a swept lock must be used: a particular comb line is guaranteed to be coupled through the cavity if the modulation depth is no less than $\lambda/2$. For example, when modulating around the main cavity resonance, the modulation depth should be set sufficiently larger than the variation in the resonance cavity length caused by dispersion, but less than $\lambda/2$ to avoid comb on cavity resonance from the side resonance. This is indicated by the purple shaded box. In actual experiments, it is not necessarily required to engage cavity swept lock to the main resonance. Side resonances can be used as well. This can be used as a strategy to counter the mirror dispersion effect to reduce the variation in resonance cavity length.

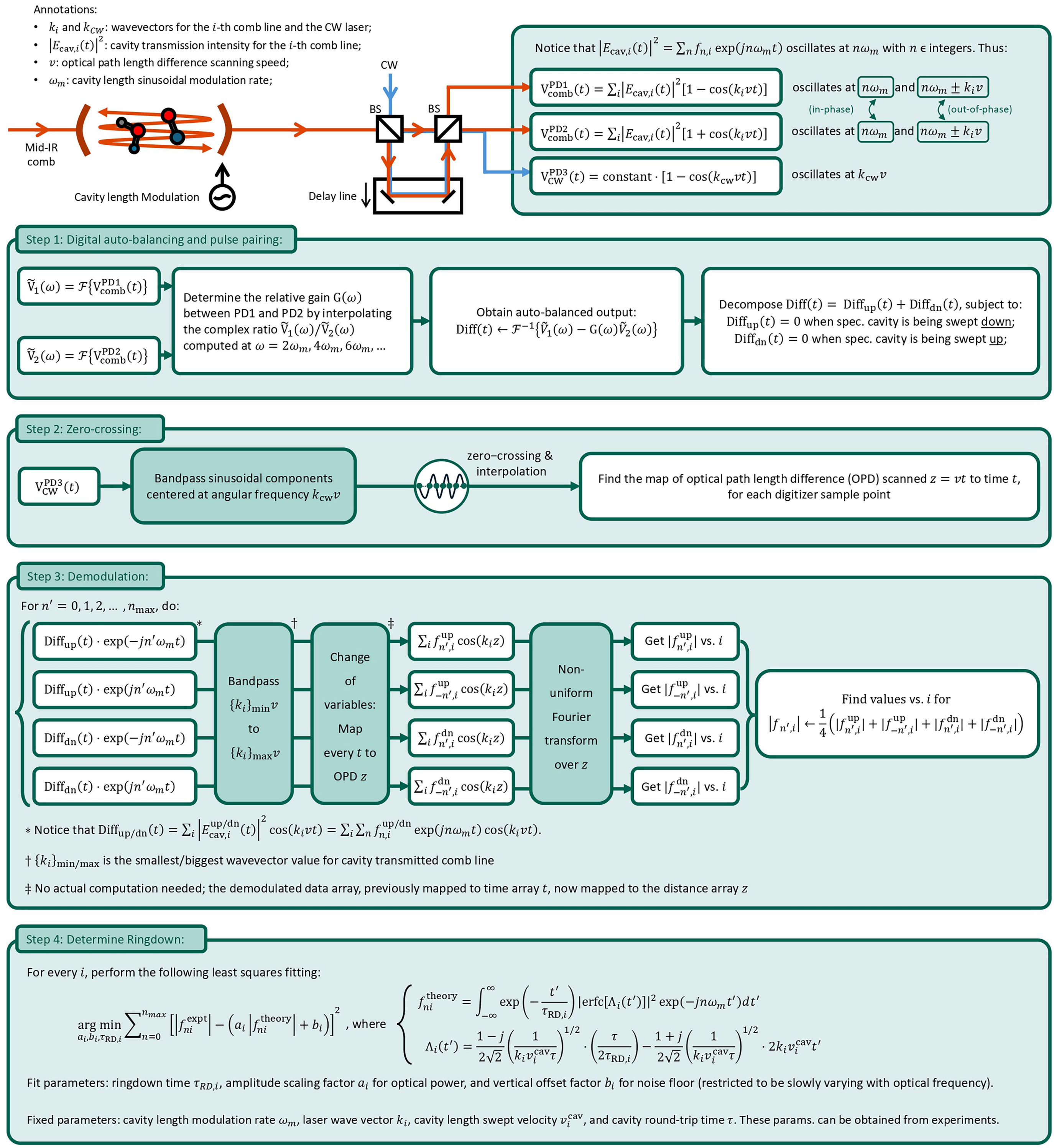

Annotations:

- $k_i$ and $k_{CW}$: wavevectors for the $i$-th comb line and the CW laser;
- $|E_{\mathrm{cav},i}(t)|^2$: cavity transmission intensity for the $i$-th comb line;
- $v$: optical path length difference scanning speed;
- $\omega_m$: cavity length sinusoidal modulation rate;

Notice that $|E_{\mathrm{cav},i}(t)|^2 = \sum_n f_{n,i} \exp(jn\omega_m t)$ oscillates at $n\omega_m$ with $n \in$ integers. Thus:

$\mathrm{V}_{\mathrm{comb}}^{\mathrm{PD1}}(t) = \sum_i |E_{\mathrm{cav},i}(t)|^2[1 - \cos(k_i v t)]$ oscillates at $\boxed{n\omega_m}$ and $\boxed{n\omega_m \pm k_i v}$

(in-phase) (out-of-phase)

$\mathrm{V}_{\mathrm{comb}}^{\mathrm{PD2}}(t) = \sum_i |E_{\mathrm{cav},i}(t)|^2[1 + \cos(k_i v t)]$ oscillates at $\boxed{n\omega_m}$ and $\boxed{n\omega_m \pm k_i v}$

$\mathrm{V}_{\mathrm{CW}}^{\mathrm{PD3}}(t) = \mathrm{constant} \cdot [1 - \cos(k_{\mathrm{cw}} v t)]$ oscillates at $k_{\mathrm{cw}} v$

**Step 1: Digital auto-balancing and pulse pairing:**

$\tilde{\mathrm{V}}_1(\omega) = \mathcal{F}\{\mathrm{V}_{\mathrm{comb}}^{\mathrm{PD1}}(t)\}$

$\tilde{\mathrm{V}}_2(\omega) = \mathcal{F}\{\mathrm{V}_{\mathrm{comb}}^{\mathrm{PD2}}(t)\}$

Determine the relative gain $\mathrm{G}(\omega)$ between PD1 and PD2 by interpolating the complex ratio $\tilde{\mathrm{V}}_1(\omega)/\tilde{\mathrm{V}}_2(\omega)$ computed at $\omega = 2\omega_m, 4\omega_m, 6\omega_m, \ldots$

Obtain auto-balanced output: $\mathrm{Diff}(t) \leftarrow \mathcal{F}^{-1}\{\tilde{V}_1(\omega) - \mathrm{G}(\omega)\tilde{V}_2(\omega)\}$

Decompose $\mathrm{Diff}(t) = \mathrm{Diff}_{\mathrm{up}}(t) + \mathrm{Diff}_{\mathrm{dn}}(t)$, subject to:
$\mathrm{Diff}_{\mathrm{up}}(t) = 0$ when spec. cavity is being swept <u>down</u>;
$\mathrm{Diff}_{\mathrm{dn}}(t) = 0$ when spec. cavity is being swept <u>up</u>;

**Step 2: Zero-crossing:**

$\mathrm{V}_{\mathrm{CW}}^{\mathrm{PD3}}(t)$

Bandpass sinusoidal components centered at angular frequency $k_{\mathrm{cw}} v$

zero–crossing & interpolation

Find the map of optical path length difference (OPD) scanned $z = vt$ to time $t$, for each digitizer sample point

**Step 3: Demodulation:**

For $n' = 0, 1, 2, \ldots, n_{\max}$, do:

$\mathrm{Diff}_{\mathrm{up}}(t) \cdot \exp(-jn'\omega_m t)$ *

$\mathrm{Diff}_{\mathrm{up}}(t) \cdot \exp(jn'\omega_m t)$

$\mathrm{Diff}_{\mathrm{dn}}(t) \cdot \exp(-jn'\omega_m t)$

$\mathrm{Diff}_{\mathrm{dn}}(t) \cdot \exp(jn'\omega_m t)$

Bandpass $\{k_i\}_{\min} v$ to $\{k_i\}_{\max} v$ †

Change of variables: Map every $t$ to OPD $z$ ‡

$\sum_i f_{n',i}^{\mathrm{up}} \cos(k_i z)$

$\sum_i f_{-n',i}^{\mathrm{up}} \cos(k_i z)$

$\sum_i f_{n',i}^{\mathrm{dn}} \cos(k_i z)$

$\sum_i f_{-n',i}^{\mathrm{dn}} \cos(k_i z)$

Non-uniform Fourier transform over $z$

Get $|f_{n',i}^{\mathrm{up}}|$ vs. $i$

Get $|f_{-n',i}^{\mathrm{up}}|$ vs. $i$

Get $|f_{n',i}^{\mathrm{dn}}|$ vs. $i$

Get $|f_{-n',i}^{\mathrm{dn}}|$ vs. $i$

Find values vs. $i$ for
$|f_{n',i}| \leftarrow \frac{1}{4}\left(|f_{n',i}^{\mathrm{up}}| + |f_{-n',i}^{\mathrm{up}}| + |f_{n',i}^{\mathrm{dn}}| + |f_{-n',i}^{\mathrm{dn}}|\right)$

* Notice that $\mathrm{Diff}_{\mathrm{up/dn}}(t) = \sum_i \left|E_{\mathrm{cav},i}^{\mathrm{up/dn}}(t)\right|^2 \cos(k_i v t) = \sum_i \sum_n f_{n,i}^{\mathrm{up/dn}} \exp(jn\omega_m t) \cos(k_i v t)$.

† $\{k_i\}_{\min/\max}$ is the smallest/biggest wavevector value for cavity transmitted comb line

‡ No actual computation needed; the demodulated data array, previously mapped to time array $t$, now mapped to the distance array $z$

**Step 4: Determine Ringdown:**

For every $i$, perform the following least squares fitting:

$$\underset{a_i, b_i, \tau_{\mathrm{RD},i}}{\arg\min} \sum_{n=0}^{n_{max}} \left[\left|f_{ni}^{\mathrm{expt}}\right| - \left(a_i \left|f_{ni}^{\mathrm{theory}}\right| + b_i\right)\right]^2 \text{, where } \begin{cases} f_{ni}^{\mathrm{theory}} = \int_{-\infty}^{\infty} \exp\left(-\frac{t'}{\tau_{\mathrm{RD},i}}\right) |\mathrm{erfc}[\Lambda_i(t')]|^2 \exp(-jn\omega_m t') dt' \\ \Lambda_i(t') = \frac{1-j}{2\sqrt{2}} \left(\frac{1}{k_i v_i^{\mathrm{cav}} \tau}\right)^{1/2} \cdot \left(\frac{\tau}{2\tau_{\mathrm{RD},i}}\right) - \frac{1+j}{2\sqrt{2}} \left(\frac{1}{k_i v_i^{\mathrm{cav}} \tau}\right)^{1/2} \cdot 2k_i v_i^{\mathrm{cav}} t' \end{cases}$$

Fit parameters: ringdown time $\tau_{RD,i}$, amplitude scaling factor $a_i$ for optical power, and vertical offset factor $b_i$ for noise floor (restricted to be slowly varying with optical frequency).

Fixed parameters: cavity length modulation rate $\omega_m$, laser wave vector $k_i$, cavity length swept velocity $v_i^{\mathrm{cav}}$, and cavity round-trip time $\tau$. These params. can be obtained from experiments.

**Extended Data Fig. 3 | A complete data processing workflow of MRCI.** The step-by-step workflow of MRCI for the processing of the raw interferogram data to obtain broadband cavity ringdown values. See Methods for details.

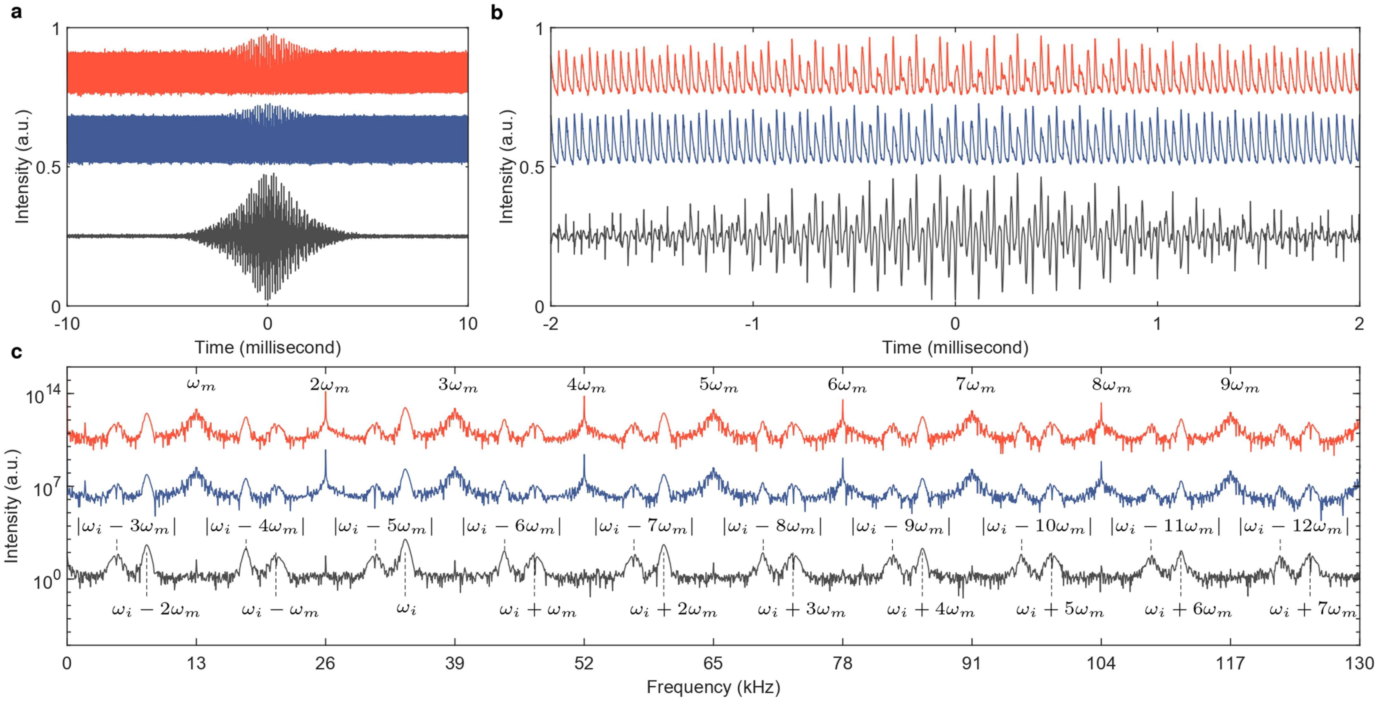

**Extended Data Fig. 4 | Interferogram data. a**, Experimental interferogram raw data collected as a function of time from the two photodetectors measuring the cavity transmitted comb light (red and blue). The black trace is the balanced output obtained from data post-processing. **b**, Zoom-in of **a** into ±2 ms. **c**, Fourier-transformed spectra for data in **a** over the time span of 20 ms. Signal carriers at $n\omega_m \pm \omega_i$ and non-cosine modulated terms at $n\omega_m$ are labelled. For these data, $\omega_m = 13$ kHz and $\omega_i \approx 34$ kHz. All traces in **a**–**c** are vertically offset for clarity.

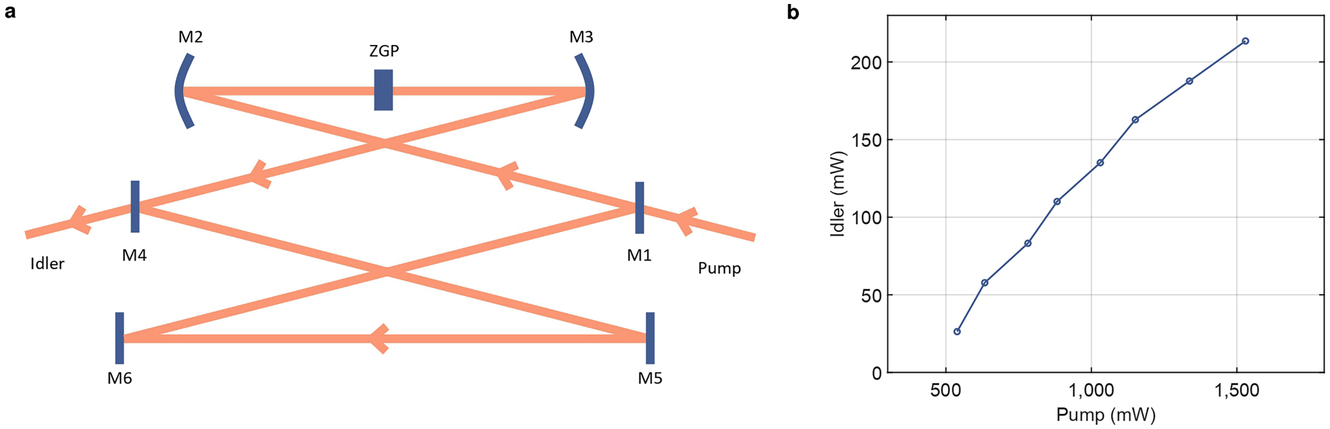

**c**

| Crystal/Mirrors | Descriptions | Coatings (Theoretical specifications) |
|---|---|---|
| ZGP | Type I @ 58 degree;<br>Height x width x length = 5 x 5 x 5 mm | Per side: $T_{avg}$ > 99 % @ 1,900-2,000 nm, $T_{avg}$ > 99% @ 2,800-3,600 nm, $T_{avg}$ > 99% @ 4,400-6,600 nm |
| M1 and M4 | Plano/Plano; ZnSe | Cavity side: T > 95 % @ 1,970 nm, $R_{avg}$ > 99.5 % @ 2,800-3,600 nm, $T_{avg}$ > 95% @ 4,600-6,400 nm;<br>Back side: T > 95 % @ 1,970 nm, $T_{avg}$ > 95% @ 4,600-6,400 nm |
| M2 and M3 | Plano/Concave @ ROC = 150 mm; AOI = 5°; Gold | $R_{avg}$ > 96 % @ 1,950-1,970 nm; $R_{avg}$ > 99.5 % @ 2,800-3,600 nm; $R_{avg}$ > 95 % @ 4,400-6,600 nm |
| M5 and M6 | Plano/Plano; Gold | |

**Extended Data Fig. 5 | The thulium–zinc germanium phosphide OPO comb.** **a**, The OPO cavity geometry. Cavity mirrors are labelled M1–M6. Pump light is injected from M1 and idler light is out-coupled from M4. Coarse and fine cavity length control are achieved with a picomotor and a piezo mounted on M5 and M6, respectively. **b**, Power dependence measured for the idler on the pump, when the idler is tuned to 2,040 cm$^{-1}$. The highest idler average power of 214 mW is measured at the pump power of 1,530 mW. The threshold pump power is 340(50) mW. Slope power efficiency is 19(1)% and photon conversion efficiency is 49(2)%. **c**, Table summarizing the crystal and mirrors specifications. AOI, angle of incidence; ROC, radius of curvature.

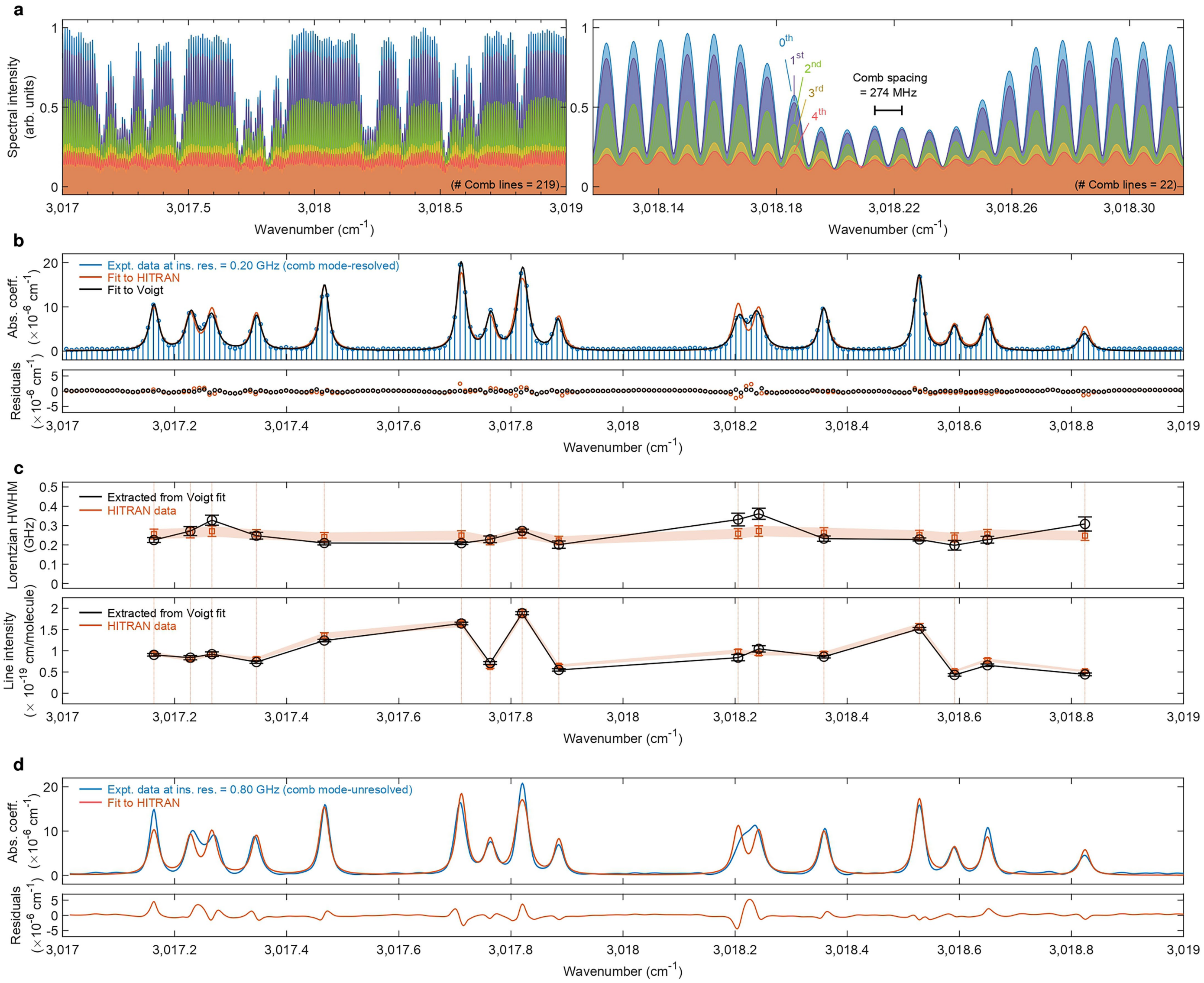

**Extended Data Fig. 6 | Cavity ringdown at comb-mode resolution.** **a**, Spectroscopy data collected at instrument resolution of 0.20 GHz for resolving the cavity transmitted comb lines spaced at 0.27 GHz frequency interval. Measurement is performed for calibrated 1.04(5) ppm $CH_4$ diluted in nitrogen at 100 Torr and 20 °C. Rovibrational absorption lines have a median width at about 0.61 GHz calculated on the basis of HITRAN data, which is considerably larger than the comb spacing. Spectroscopy data are an average from a total of 256 interferograms collected at 7.5 s each. Zero padding is used to oversample at one-tenth of the instrument resolution to accurately locate the comb line frequencies. Only the leading five Fourier harmonics are plotted for clarity. The right panel is the zoom-in to near 3,018.22 $cm^{-1}$. **b**, Ringdown absorption data determined from **a**. Stem lines in blue highlight the absorption coefficients measured by different comb lines. The data spanning 2 $cm^{-1}$ coverage uniformly sampled by 219 comb lines is globally fitted to the HITRAN database plotted in orange. Fitted concentration yields 0.97(5) ppm. We further fit each rovibrational absorption line to a Voigt profile (black). For this analysis, Gaussian linewidths are fixed at the calculated values based on HITRAN data at 20 °C. Fitted concentration is used as the true methane concentration. **c**, Molecular parameters for the Lorentzian half width at half maximum (HWHM) widths and line intensities are determined for individual rovibrational absorption lines. Experimental data in black are compared with HITRAN data in orange. Uncertainties in the HITRAN database for which linewidths reported at about 10% and line intensities at about 5% are indicated. Vertical orange dashed lines are a guide to the eye aligning extracted molecular parameters to their corresponding rovibrational absorption lines. **d**, Spectroscopy data collected at the modest instrument resolution of 0.80 GHz. In contrast to the measured data at comb-mode resolution in **b**, the two close-lying rovibrational absorption lines near 3,018.2 $cm^{-1}$ are less robustly resolved owing to the larger spectral resolution. Global fit to the HITRAN database yields 1.00(5) ppm fitted concentration for methane. To summarize, our data confirm: (1) both 0.80 GHz modest resolution or comb-mode resolution yield measured concentrations in good agreement with the calibrated value and (2) at comb-mode resolution, molecular parameters further extracted for absorption linewidths and line intensities are also in good agreement with the reported values from the HITRAN database.